THE ASTROPHYSICAL JOURNAL, 551:747–763, 2001 April 20

THE STRUCTURE OF FOUR MOLECULAR CLOUD COMPLEXES IN THE BU-FCRAO MILKY WAY GALACTIC RING SURVEY

ROBERT SIMON, JAMES M. JACKSON, DAN P. CLEMENS, AND T. M. BANIA
Institute for Astrophysical Research, Boston University, 725 Commonwealth Avenue, Boston, MA 02215; simonr@chub.bu.edu, jackson@slime.bu.edu, clemens@bu.edu, bania@ninkasi.bu.edu

AND

MARK H. HEYER
Five College Radio Astronomy Observatory and Department of Physics and Astronomy, Lederle Graduate Research Tower, University of Massachusetts, Amherst, MA 01003; heyer@fermat.astro.umass.edu
Received 2000 August 29; accepted 2000 December 22

ABSTRACT

We present a study of the structure of four molecular clouds from the Milky Way Galactic Ring Survey (GRS), a Boston University and Five College Radio Astronomy Observatory collaboration. The GRS is a new high-resolution survey in the ^{13}CO $J = 1 \rightarrow 0$ spectral line of the inner Galaxy and the 5 kpc ring, the Milky Way's dominant star-forming structure. Because of the smaller line widths of ^{13}CO compared to ^{12}CO, we can avoid velocity crowding and establish accurate kinematic distances to the clouds. The kinematic distance ambiguity in the first Galactic quadrant is resolved using self-absorption in complementary high-resolution atomic hydrogen data. The four clouds are selected to span a large range of star formation activity, from the quiescent cloud GRSMC 45.60+0.30, which shows no signs of high-mass star formation, to W49, the most luminous star-forming region in the Galaxy. We use a three-dimensional Gaussian clump decomposition to identify clumps in the clouds and to investigate their properties. Each cloud has the same clump mass spectrum, $dN/dM \propto M^{-1.8}$, independent of star formation activity. We do not find significant differences in the slopes of the relations of density, line width, and clump mass as a function of clump size among the clouds. The size-density and size–line width relations show considerable scatter. Compared to the conventional Larson scaling laws, we find systematically flatter slopes for the size-density and size–line width relations and a higher power-law index for the size-mass relation. In particular, the clump line widths for the most quiescent cloud GRSMC 45.60+0.30 are independent of clump size. While the clouds as a whole are gravitationally bound, most of the clumps are not; only a small fraction of the total number of clumps is self-gravitating. The active star-forming clouds have a higher fraction of gravitationally bound clumps and a higher mean cloud volume density than the more quiescent clouds. The gravitationally unbound clumps are possibly confined by the weight of the self-gravitating complex. The pressures needed to bind these clumps are largest for the active star-forming clouds, which have a much higher weight than the quiescent clouds. Alternatively, a high number of the gravitationally unbound clumps may be transient.

Subject headings: Galaxy: general — ISM: clouds — ISM: molecules — ISM: structure — radio lines: ISM — surveys

1. INTRODUCTION

When observed at increasingly higher linear resolution, molecular clouds reveal a rich structure of clumps and filaments. First noticed from the low volume filling factors inferred toward warm and dense cores (Ho & Townes 1983; Snell et al. 1984; Evans et al. 1987), hierarchical, clumpy structures in molecular clouds are directly confirmed by observations (Kramer et al. 1998; Heithausen et al. 1998). Additional indirect evidence for clumpy molecular clouds is the observed large extent of [C II] 158 μm emission, the observed ^{12}CO/^{13}CO and [C II]/CO line ratios (which can only be modeled by radiative transfer through a clumpy medium; Störzer, Stutzki, & Sternberg 1996), and the smooth line profiles of optically thick molecular transitions (e.g., Martin, Hills, & Sanders 1984; Tauber, Goldsmith, & Dickman 1991). The observed properties of the clouds and the clump ensembles yield important information about the effects of turbulence and self-gravity, which generate cloud substructure and affect the process of star formation itself.

Several approaches to describe and quantify clumpiness of molecular clouds have been established. The most straightforward technique is to decompose the observed spectral line data cubes or continuum images into discrete clumps. The method developed by Stutzki & Güsten (1990) models the three-dimensional (two spatial and one velocity) data as Gaussian-shaped clumps. Other algorithms identify clumps as closed surfaces in position-velocity space (e.g., Williams, De Geus, & Blitz 1994; Heyer, Carpenter, & Snell 2001). Once the clumps are identified, general trends in their properties (e.g., mass, size, density, and line width) are used to characterize cloud structure. Following the approach of Larson (1981), many studies applying different methods to identify clumps arrive at similar results showing a power-law distribution of clump density, line width, or mass as a function of clump size (e.g., Leung, Kutner, & Mead 1983; Sanders, Scoville, & Solomon 1985; Dame et al. 1986; Kramer, Stutzki, & Winnewisser 1996; Heithausen 1996; Heyer & Schloerb 1997; Williams, Blitz, & McKee 2000). Moreover, the clump mass spectra reveal a power-law distribution $dN/dM \propto M^{-\alpha_M}$, with α_M in the range 1.5–1.9 over several orders of magnitude in clump mass (Elmegreen & Falgarone 1996; Heithausen et al. 1998; Kramer et al. 1998).

Besides the direct approach of decomposing the observed

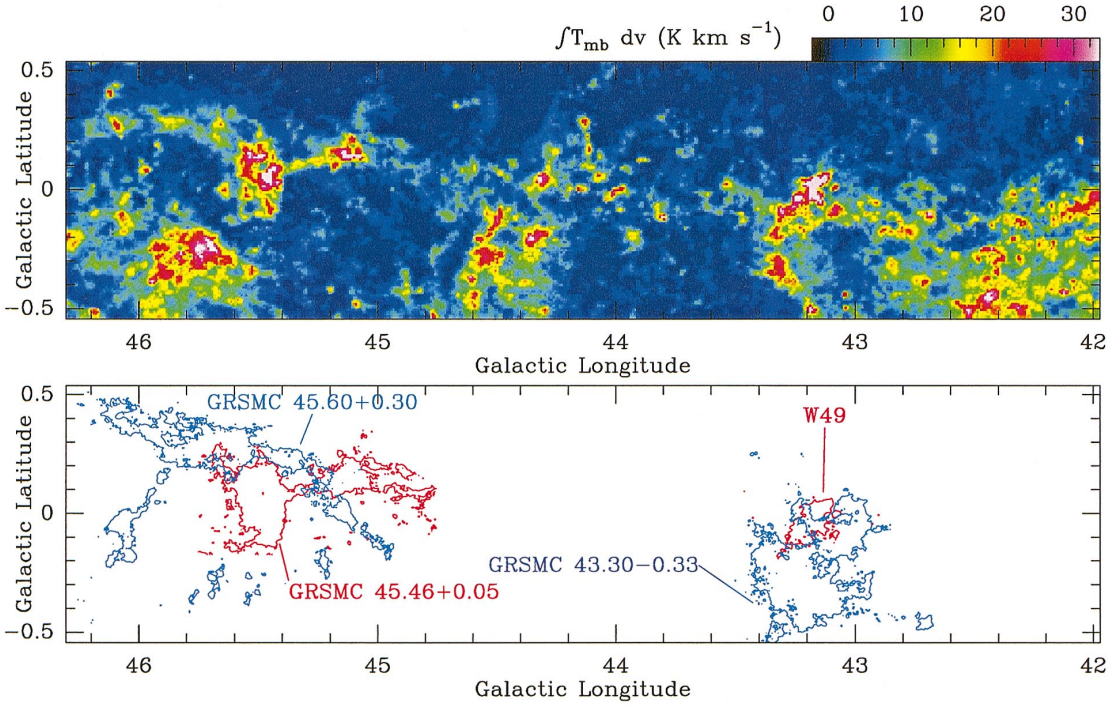

FIG. 1.—Zeroth-moment map of GRS ^{13}CO emission integrated from −5 to 80 km s^{-1} (*top panel*). The map was constructed following the procedure described by Adler et al. (1992). The transfer function ranges from −2 to 33 K km s^{-1} on a linear scale. The peak integrated intensities of the moment image are located within a small area of W49 (the maximum value is 159 K km s^{-1}). The plot range has been chosen in order to enhance lower intensity features in the map. The bottom panel outlines the four cloud complexes selected as described in § 3. Blue contours correspond to the 6 σ level in the two near clouds GRSMC 45.60+0.30 and GRSMC 43.30−0.33, and red contours outline the 9 σ level in the two distant clouds GRSMC 45.46+0.05 and W49 for intensities integrated over the clouds' velocity range of emission (see Fig. 2 and § 3).

emission into clumps, a number of mathematical tools are used to study the spatial and kinematic structure of clouds. The observed self-similarity over orders of magnitude in linear scales, the power-law behavior of the clump mass spectra, and the important role played by turbulence in the dynamics of molecular clouds lead to the use of fractals to describe cloud structure (e.g., Falgarone, Phillips, & Walker 1991; Vogelaar & Wakker 1994; Stutzki et al. 1998). Promising approaches to analyzing the observed velocity fields in spectral line data include the principal component analysis introduced by Heyer & Schloerb (1997), the probability density functions of centroid velocity fluctuations (Miesch, Scalo, & Bally 1999), and the spectral correlation function as a measure of similarity between neighboring spectra (Rosolowsky et al. 1999).[1]

Most previous cloud decomposition studies have examined molecular regions within the solar neighborhood or the outer Galaxy. Most of the molecular gas of the Milky Way, however, resides in the inner Galaxy, where the environmental conditions may be quite distinct. To evaluate the internal structure of giant molecular clouds (GMCs) in this region of the Galaxy, we have analyzed four molecular cloud complexes within a new ^{13}CO survey data set. The clouds were selected to span a large range in mass and star formation activity. We use the clump decomposition algorithm of Stutzki & Güsten (1990) to identify clumps and their properties.

The Boston University–Five College Radio Astronomy Observatory (BU-FCRAO) Milky Way Galactic Ring Survey (GRS) is a new study of ^{13}CO $J = 1 \rightarrow 0$ line emission from the molecular clouds in the first Galactic quadrant. Since the GRS covers large areas of the sky on a completely sampled grid, with high angular and spectral resolution, it constitutes a superb database to investigate molecular cloud structure within the first Galactic quadrant. Previous large-scale surveys that covered this region of the Milky Way include the Columbia 1.2 m survey (Dame et al. 1986, 1987), the UMass Stony Brook survey (UMSB; Sanders et al. 1986) in ^{12}CO $J = 1 \rightarrow 0$, and the Bell Labs 7 m survey (Stark et al. 1988) in ^{13}CO $J = 1 \rightarrow 0$. These studies reveal the distribution and global properties of the molecular gas in the inner Milky Way but, unlike the GRS, are limited by low angular resolution or severe undersampling and cannot detect or resolve small-scale cloud structure.

The outline of this paper is as follows. A summary of the observing procedure and the observational parameters for the GRS data set is given in § 2, together with an integrated intensity image of the data. In § 3 we describe the criteria for the selection of the clouds and give their positions and distances. After introducing the clump decomposition method and the determination of the physical parameters of the clumps in § 4, we present the results for the individual clouds in § 5. The results are discussed in § 6, which is followed by a summary of the conclusions in § 7.

2. THE GALACTIC RING SURVEY DATA

The GRS observations presented in this paper were obtained with the FCRAO 14 m telescope between 1998 December and 1999 May. A field of over 4 deg^2 from $l =$ 42.°0 to 46.°3 and $b = -0.°5$ to 0.°5 was observed in the ^{13}CO $J = 1 \rightarrow 0$ transition at 110.201 GHz. We used the FCRAO 16 element array receiver SEQUOIA, which provided a

[1] For detailed summaries of the different methods and results on cloud structure see the reviews by Stutzki (1998) and Williams et al. (2000).

mean receiver noise temperature of 80 K. Typical system noise temperatures ranged between 200 and 300 K.

The spectrometer consisted of 16 autocorrelators, each with a bandwidth of 40 MHz, 512 channels, and a channel spacing of 0.21 km s^{-1}. The actual FWHM velocity resolution of the autocorrelators is 0.26 km s^{-1}. The resulting bandwidth of 110 km s^{-1} was sufficient to cover all ^{13}CO emission at positive LSR velocities for Galactic longitudes above 40°. The spectra were calibrated using a vane to switch between emission from the sky and an ambient temperature load. All intensities are reported on a main-beam brightness temperature scale, T_{mb}, using the main-beam efficiency $\eta_{mb} = 0.48$ as derived from observations of planets.

The observations were obtained in a position-switching mode, where four consecutive array pointings toward target regions shared the same off-source reference integration. Integration times for one target pointing ranged between 10 and 20 s. Most targets were observed twice to achieve the desired sensitivity. The resulting spectra have a mean baseline noise level (rms main-beam temperature) of 0.48 K per 0.21 km s^{-1} channel.

Sky positions free of emission were selected by using data from the Columbia ^{12}CO $J = 1 \rightarrow 0$ survey (T. M. Dame 1998, private communication). These potential off-source positions, chosen to be as close as possible to the Galactic plane, were then checked for emission in ^{13}CO by position-switched observations against positions from the Columbia survey known to be free of emission in ^{12}CO to an rms noise level of 0.05 K (0.65 km s^{-1} channel) in an 8′ beam. No ^{13}CO emission was found toward the GRS off-source positions above a noise level of $\Delta T_{mb} \sim 0.15$ K.

A map of ^{13}CO $J = 1 \rightarrow 0$ intensity integrated over the velocity range from -5 to 80 km s^{-1} is shown in Figure 1. The FWHM beam size of the telescope is 46″ at the ^{13}CO frequency, and the data set comprises a total of 124,000 positions on a 22″ grid. The map was constructed following the masked moment procedure described by Adler et al. (1992) using a temperature threshold of 0.52 K, i.e., slightly higher than the mean 1 σ level of the data.

3. SELECTION OF CLOUDS FROM THE SURVEY

From the survey region shown in Figure 1, we selected four clouds that are isolated in space and velocity, span a wide range of star formation activity, and for which we could determine accurate distances. The coordinates of the clouds and distances from the Sun and the Galactic center are summarized in Table 1. Clouds without a commonly used designation are named according to their Galactic longitude and latitude with the prefix GRSMC, referring to Galactic Ring Survey Molecular Cloud.

GRSMC 45.60+0.30 is the most quiescent of the four clouds, showing typical line widths of 1 km s^{-1}. The observed ^{13}CO lines are slightly broader toward GRSMC 43.30−0.33, typically 3 km s^{-1}. Several *IRAS* point sources lie within the regions covered by ^{13}CO emission for both of these clouds. Most of these infrared sources either are located outside the boundaries of the clouds or have unambiguous molecular emission counterparts in velocity channels outside the range relevant for the selected clouds. They are thus not associated with the two quiescent clouds but located at different distances. A small number of *IRAS* point sources inside the cloud boundaries have multiple or no clear ^{13}CO emission peak counterparts over the complete velocity range covered by the GRS observations. According to the selection criteria of Wouterloot et al. (1990), their colors are not typical for embedded star-forming regions. We therefore conclude that neither cloud is forming high- or intermediate-mass stars.

Both GRSMC 45.46+0.05 (Testi, Felli, & Taylor 1999) and W49 (e.g., Welch et al. 1987) are known sites of active, high-mass star formation, and a number of ^{13}CO emission peaks in the velocity range of the clouds have *IRAS* point-source counterparts that satisfy the above color criteria for star-forming regions.

Although W49 and GRSMC 43.30−0.33, as well as GRSMC 45.60+0.30 and GRSMC 45.46+0.05, cover regions along almost identical lines of sight, they are well separated in velocity and hence in distance. Since the zeroth-moment map shown in Figure 1 contains the emission integrated over the complete velocity range, details for the individual clouds are difficult to discern. Therefore, individual maps integrated over the narrower velocity ranges for each cloud are shown in Figure 2.

Accurate estimates of the distances to the clouds are crucial to determine sizes and masses for the clumps inside the clouds. The distance to W49 is 11.4 kpc, as determined from proper motions of H_2O masers (Gwinn, Moran, & Reid 1992). Kinematic distances to the other three clouds were derived using the Galactic rotation curve of Clemens (1985), $(R_0, \theta_0) = (8.5$ kpc, 220 km $s^{-1})$. In the first Galactic quadrant, however, the kinematic distance is double valued, except for clouds at the tangent point. The cloud GRSMC 45.46+0.05 has a centroid LSR velocity of 60 km s^{-1}, near the tangent point velocity for $l = 45.^{\circ}5$, which places it at a kinematic distance of 6 kpc. The distance ambiguity for the two clouds GRSMC 45.60+0.30 and GRSMC 43.30−0.33 is resolved using complementary atomic hydrogen data from the Boston University Arecibo Observatory (BUAO) H I Survey of the Galactic plane (T. M. Bania et al. 2001, in preparation). Since H I is ubiquitous in the Galaxy, it provides a large-scale warm background throughout the

TABLE 1

MOLECULAR CLOUDS SELECTED FOR THIS STUDY

Cloud[a]	l (deg)	b (deg)	v_{LSR} (km s^{-1})	Distance (kpc)	Galactocentric Radius (kpc)
GRSMC 45.60+0.30.....	45.60	0.30	25.0	1.8[b]	7.0
GRSMC 43.30−0.33.....	43.30	−0.33	40.0	3.0[b]	6.5
GRSMC 45.46+0.05.....	45.46	0.05	60.0	6.0[b]	6.0
W49.....	43.17	0.00	11.2	11.4[c]	8.5

[a] Cloud coordinates denote the position of a prominent ^{13}CO emission peak.
[b] Distance determined kinematically; see text.
[c] Distance adopted from Gwinn et al. 1992.

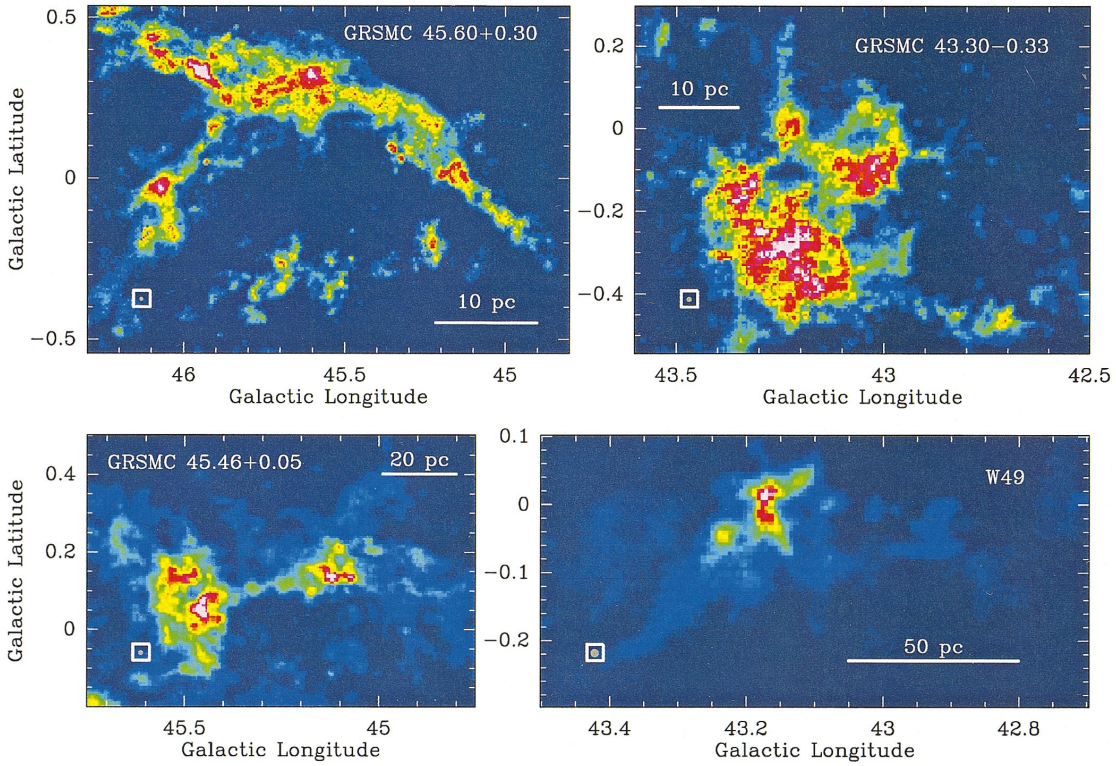

FIG. 2.—Color-scale representation of zeroth-moment maps of the GRS ^{13}CO intensity integrated over the velocity range relevant for emission from the individual cloud complexes. The beam size is indicated as a filled circle in the lower left corner of each panel. The linear size scales were determined assuming the distances given in Table 1. The plot intensity ranges are as follows. *Top panels:* Quiescent clouds; ^{13}CO integrated intensity from 0.5 to 6.1 K km s^{-1} for GRSMC 45.60+0.30 (*left panel*; v_{LSR} = 20–30 km s^{-1}) and from 0.5 to 9.7 K km s^{-1} for GRSMC 43.30−0.33 (*right panel*; v_{LSR} = 35–50 km s^{-1}). *Bottom:* Star-forming clouds; ^{13}CO integrated intensity from 0.5 to 47.4 K km s^{-1} for GRSMC 45.46+0.05 (*left panel*; v_{LSR} = 50–70 km s^{-1}) and from 0.5 to 111.3 K km s^{-1} for W49 (*right panel*; v_{LSR} = −5–25 km s^{-1}).

Galactic plane. Colder foreground clouds will be seen in H I self-absorption toward this background at the LSR velocity of the molecular cloud. Using this technique, Jackson et al. (2001) show that both GRSMC 45.60+0.30 and GRSMC 43.30−0.33 have H I self-absorption at the LSR velocity of the ^{13}CO $J = 1 \rightarrow 0$ line, and hence the two clouds are located at the near distances. Consequently, we assigned the near kinematic distances of 1.8 and 3.0 kpc to the clouds GRSMC 45.60+0.30 and GRSMC 43.30−0.33, respectively. The fact that both clouds cover large solid angles independently suggests the near distance.

4. CLUMP DECOMPOSITION AND CLUMP PARAMETERS

The first step in our analysis of cloud structure was to identify clumps in the clouds and to derive their basic properties including sizes, line widths, and masses. The *GAUSSCLUMPS* algorithm (Stutzki & Güsten 1990) is used to decompose emission from data cubes into Gaussian-shaped clumps in (l, b, v)-space by successively finding the emission peak, fitting a three-dimensional Gaussian clump to it, and subtracting the fitted clump from the cube before iterating on the residual cube.

If the data set is undersampled, *GAUSSCLUMPS* fits a high number of low-mass clumps of the size of the resolution element (Kramer et al. 1998). *GAUSSCLUMPS* is most effective when applied to data that are fully sampled in all three dimensions. Consequently, we smoothed and resampled the velocity axis to a fully sampled 0.25 km s^{-1} channel spacing and 0.5 km s^{-1} spectral resolution. The resulting rms noise is 0.34 K per 0.25 km s^{-1} channel on a T_{mb} scale. No spatial smoothing or resampling was necessary since the data were obtained on a fully sampled spatial grid (22″ sampling, 46″ beam size). The clump decomposition was ceased when the peak intensity of a newly identified clump dropped below 3 times the rms noise value.

The clump decomposition provides the positions, LSR center velocities, and orientations of the individual clumps, as well as intrinsic (i.e., deconvolved from the resolution) quantities such as the clump sizes, brightness temperatures, and line widths. Before deconvolving to intrinsic quantities, we discarded objects with fitted sizes smaller than 130% of our spatial and spectral resolutions (i.e., intrinsic sizes smaller than ∼80% of the resolution) since *GAUSSCLUMPS* tends to approximate the irregular shapes of the lower level intensity distribution by a large number of small, low-mass clumps that cannot be reliably deconvolved. For a clump mass spectrum $dN/dM \propto M^{-\alpha_M}$ with a power-law index $\alpha_M < 2$, the high-mass end of the distribution dominates the total mass. As shown by Kramer et al. (1998), excluding a large number of small-size clumps does not change the slope of the clump mass spectrum. That same paper contains a thorough discussion of the stability of the results to variation of the input parameters for the decomposition program. Following this discussion and using their methods to test our results, we elected to use the same standard set of input parameters they use for the decomposition of their Orion B data, namely, $s_0 = s_a = s_c = 1$ and $w = 3$ (see Kramer et al. 1998 for details).

The ^{13}CO clump column densities were determined using the ^{13}CO clump brightness temperatures T_{mb} in K and

FWHM line widths Δv in km s^{-1} in the optically thin, thermalized limit. The excitation temperature was fixed at 10 K. The use of a constant ^{13}CO excitation temperature of 10 K is justified by ^{12}CO results obtained from the UMSB survey at similar angular resolution: the peak ^{12}CO $J = 1 \rightarrow 0$ brightness temperatures observed toward all four clouds are typically $\sim$10 K, which, under the assumption of optically thick ^{12}CO emission filling the beam, is approximately T_{ex}. Moreover, the derived ^{13}CO column densities and masses are only weakly sensitive to the exact choice of the excitation temperature. Changing T_{ex} to 20 or 30 K increases the derived mass by 40% and 92%, respectively.

The total ^{13}CO clump column density in cm^{-2} is given by

$$N(^{13}\mathrm{CO}) = 8.75 \times 10^{14} T_{mb}\, \Delta v\ . \quad (1)$$

The total mass of a clump depends on this ^{13}CO column density, the abundance of ^{13}CO relative to H_2, the clump's solid angle, and the distance to the cloud. We applied conversion factors of $R(^{12}\mathrm{CO}/^{13}\mathrm{CO}) = 45$ adopted from Langer & Penzias (1990) (this is a mean value for Galactocentric radii between 4 and 8 kpc) and $X(^{12}\mathrm{CO}/\mathrm{H_2}) = 8 \times 10^{-5}$ (Blake et al. 1987), as well as a correction to the hydrogen mass of a factor of 1.36 to account for helium and other heavy elements (Allen 1973). The clump hydrogen column density in cm^{-2} is then

$$N(\mathrm{H_2}) = 4.92 \times 10^{20} T_{mb}\, \Delta v\ , \quad (2)$$

and the clump mass in units of solar masses is

$$M_{LTE} = 3.05 \times 10^{-25} N(^{13}\mathrm{CO}) \theta_x\, \theta_y\, D^2\ , \quad (3)$$

where θ_x and θ_y are the sizes of the principal half-axes of the clump in arcseconds and D is the distance to the cloud in pc. Normalized to a 1 K km s^{-1} line, a distance of 1 kpc, and a 60″ clump size, this yields

$$M_{LTE} = 0.96\ M_\odot \left[\frac{N(^{13}\mathrm{CO})}{8.75 \times 10^{14}\ \mathrm{cm^{-2}}}\right]\left(\frac{\theta_x}{60''}\right)\left(\frac{\theta_y}{60''}\right)\left(\frac{D}{\mathrm{kpc}}\right)^2\ . \quad (4)$$

Ratios of ^{12}CO (from the UMSB survey) to GRS ^{13}CO line intensities for the same positions are typically in the range 2–5. Under the assumption of optically thick ^{12}CO emission, this suggests only a moderate optical depth in the ^{13}CO $J = 1 \rightarrow 0$ transition. Therefore, we did not correct the clump masses for opacity effects in the ^{13}CO line. Subthermal excitation of higher rotational levels may result in an overestimate of total column densities in the optically thin, thermalized limit. This overestimate of the column density, however, is of the same order as the underestimate due to a moderate opacity in the observed low-J transition. Given the above assumptions for the excitation and opacity for the ^{13}CO $J = 1 \rightarrow 0$ line, the derived column densities, and hence masses, are lower limits and estimated to be accurate to within a factor of a few.

5. RESULTS

5.1. *Cloud Properties*

The global cloud properties are summarized in Table 2. Total masses of the cloud complexes were determined from the observed ^{13}CO intensity above the 3 σ level integrated over the relevant velocity range and the area of the cloud (M_{int}^{cloud}). These masses were derived using the same assumptions on optical depth, excitation, and conversion to H_2 as described in the previous section. The total masses of the cloud complexes range from a few times $10^4\ M_\odot$ for the two near, more quiescent clouds up to $5 \times 10^5\ M_\odot$ for the two active star-forming clouds.

The cloud masses recovered by *GAUSSCLUMPS* (M_{GC}^{cloud}) were calculated from the sum of the masses of the individual clumps. Typically 60%–70% of the cloud masses M_{int}^{cloud} are decomposed into reliable clumps.

Estimates of the virial masses of the cloud complexes M_{vir}^{cloud} strongly depend on the cutoff intensity level and the method used to determine the cloud radius. Ungerechts, Umbanhowar, & Thaddeus (2000) showed that the intensity-weighted average $\langle R \rangle = \sum_i W_i r_i / \sum_i W_i$, where W_i is the integrated intensity of pixel i, together with a cutoff intensity level of 10% of the peak integrated intensity or lower, yields more reliable cloud radii than the geometric radius $r_g = (A/\pi)^{1/2}$ computed from the area A enclosed by the cutoff contour. We obtained intensity-weighted cloud radii $\langle R \rangle$ (col. [9] of Table 2) by summing over all cloud positions with integrated intensity above the mean 3 σ level and radii r_i measured relative to the integrated intensity centroid. Because of the limited dynamic range of the integrated intensities in GRSMC 45.60+0.30, the 3 σ level for this cloud is at $\sim$17% of its peak integrated intensity, which may result in a slight underestimate of the cloud radius. For the other three clouds, the 3 σ level is below the 10% level of the peak integrated intensity from the cloud and meets the above criterion.

As also shown by Ungerechts et al. (2000), this choice of $\langle R \rangle$ in the calculation of the virial mass $M_{vir}^{cloud} = k_{vir} \langle R \rangle \Delta v^2$ has the additional advantage that the factor k_{vir}, which accounts for different density distributions [power

TABLE 2

CLOUD CHARACTERISTICS

Cloud (1)	N_{sel} (2)	M_{int}^{cloud} ($10^4\ M_\odot$) (3)	M_{GC}^{cloud} ($10^4\ M_\odot$) (4)	$M_{GC}^{cloud}/M_{int}^{cloud}$ (5)	M_{vir}^{cloud} ($10^4\ M_\odot$) (6)	$M_{vir}^{cloud}/M_{int}^{cloud}$ (7)	Δv_{cloud} (km s^{-1}) (8)	$\langle R \rangle$ (pc) (9)	$\langle n_{H_2} \rangle$ (cm^{-3}) (10)
GRSMC 45.60+0.30.....	235	1.7	1.2	0.70	2.1	1.2	2.2	13	30
GRSMC 43.30−0.33.....	247	6.1	3.3	0.55	8.2	1.3	4.3	13	100
GRSMC 45.46+0.05.....	406	49	34	0.69	126	2.6	11.5	29	80
W49.....	85	48	32	0.67	102	2.1	11.7	22	160

NOTE.—Masses of the cloud complexes were estimated from the observed integrated ^{13}CO intensity (col. [3]), from the sum of the individual masses of the selected clumps identified by *GAUSSCLUMPS* (col. [4]; the number of clumps used is given in col. [2]), and the virial mass of the complex (col. [6]) $M_{vir}^{cloud} = 340 \langle R \rangle \Delta v_{cloud}^2$ as discussed in the text. For this we used the FWHM line width Δv of the spectrum averaged over the face of the cloud (col. [8]) and the cloud radius $\langle R \rangle$ in pc (col. [9]). The percentage of mass recovered by *GAUSSCLUMPS* compared to M_{int}^{cloud} is given in col. (5). We also included the ratio of virial mass to ^{13}CO mass of the individual clouds (col. [7]) and mean hydrogen molecule densities (col. [10]).

laws of the form $\rho_n(r) \propto r^{-n}$ ($n = 0, 1, 2$), exponential, and Gaussian], depends only weakly on the assumed density law. For the virial cloud masses included in Table 2 we used $k_{\rm vir} = 340$, which is within 6% of the value for each of these density laws.

The mean densities of the clouds listed in Table 2 were calculated from $M_{\rm int}^{\rm cloud}$ and the volume of a sphere with the cloud radius as listed in Table 2.

5.1.1. *W49: Contamination by Near Molecular Gas*

To derive the clump parameters, we implicitly assume that all of the emission in the specified velocity range originates from a single molecular cloud and at one distance. At a given LSR velocity, the emission from a GMC at the far side of the Galaxy, however, may be significantly contaminated by unrelated material at the near kinematic distance. In this case, the masses and sizes of near clumps will be significantly overestimated if we use the kinematic distance of the far cloud. The opposite case, in which emission from a near cloud contains some contribution from gas at the far distance, is less problematic since the mass and size of a far clump calculated for the near distance will be significantly underestimated and will therefore not bias the total mass or mass spectrum estimated for the near complex. Since W49 is located at the far kinematic distance, it is important to ascertain whether any of the clumps identified by the clump decomposition are located in front of W49 at the near distance.

The near kinematic distance for an LSR velocity of 10 km s^{-1} is $\sim$1 kpc. Any massive star-forming region at this distance would cover a much larger area of the sky than W49 and would have comparable integrated intensity or be much brighter. We certainly do not see such a cloud along the line of sight toward the W49 region in the relevant velocity range of our ^{13}CO data.

Low-density, quiescent material at the near distance could produce enough brightness in a narrow line to permit distinguishing it from W49 emission. The ^{13}CO spectrum shown in the top panel of Figure 3 was obtained by averaging over the region shown in the bottom panel. It reveals broad emission between 0 and 20 km s^{-1} and a narrow ($\Delta v = 1.1$ km s^{-1}), intense feature at a velocity of 16 km s^{-1}. A three-component Gaussian fit was applied to the spectrum, two components to model the broad emission associated with W49 and one component for the narrow 16 km s^{-1} line. The results of the fits are superposed to the spectrum. The relatively high intensity and small line width of the 16 km s^{-1} component compared to the broad emission from W49 imply that this material lies at the near kinematic distance.

H I spectra from the BUAO survey toward positions away from the strong W49 continuum show self-absorption at exactly the velocity of the peak of the narrow ^{13}CO line. Following the conclusions of Jackson et al. (2001), this places the clumps associated with this spectral feature at the near kinematic distance. We therefore conclude that emission along the line of sight toward W49 is partially contaminated by emission from nearby molecular gas at a velocity of 16 km s^{-1}.

This conclusion is further supported by the unusual properties of some of the clumps seen in the channel map integrated from $v_{\rm LSR} = 15$ to 17 km s^{-1} (Fig. 3, *bottom panel*). If these clumps actually lie at the same distance as W49, then many of them have large apparent distances

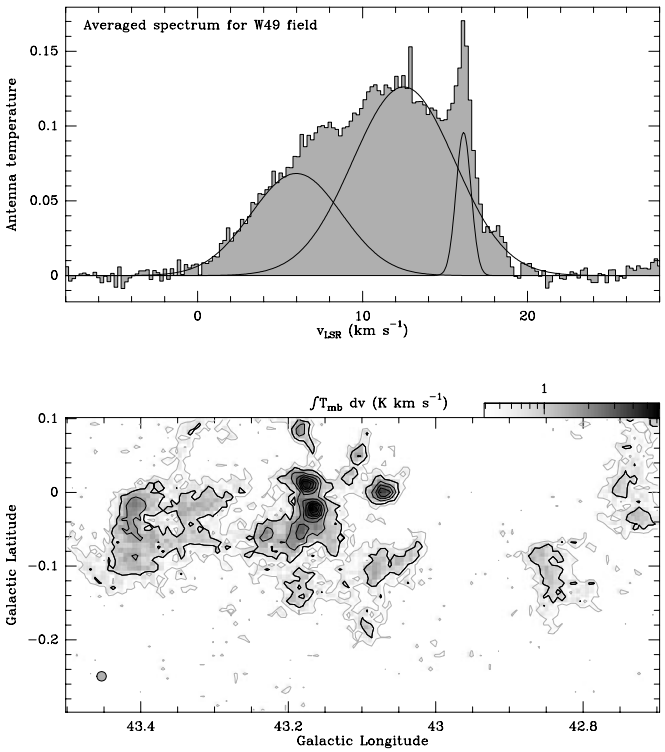

FIG. 3.—Emission associated with gas at the near kinematic distance toward the W49 region. The gray filled histogram in the top panel shows the ^{13}CO $J = 1 \rightarrow 0$ spectrum averaged over the region shown in the bottom panel. A Gaussian fit for two broad components and one narrow line was applied to model the emission from W49 and the near gas. The fit results are shown superposed on the spectrum. The bottom panel displays the ^{13}CO $J = 1 \rightarrow 0$ intensity integrated over the velocity range from 15 to 17 km s^{-1}, relevant for emission from the near gas, toward the W49 region. The beam size is indicated in the lower left corner.

($\sim$50 pc) from the center of W49 [(l, b) $\sim$ (43.15, $-$0.05)], large apparent clump sizes (up to 7 pc), and large masses (of the order of 10^3 $M_\odot$). Emission associated with the narrow component is inconspicuous in the image of the total integrated intensity (see Fig. 2), which is dominated by broad emission from W49.

In order to minimize confusion with this near material toward W49, all clumps with centroid velocities between 14.5 and 17.5 km s^{-1} were excluded from the following analysis.

5.2. *Clump Mass Spectra*

The masses for clumps identified by *GAUSSCLUMPS* were binned for each individual cloud to yield the clump mass spectra shown in Figure 4. Because the decomposition misses smaller, less massive clumps in the distant clouds, the clump masses cover slightly different mass ranges for each cloud. The clump masses span 2 orders of magnitude for an individual cloud and almost 4 orders of magnitude for the combined data set from 5 $M_\odot$ in GRSMC 45.60+0.30 to 30,000 $M_\odot$ for the most massive clumps in W49.

The minimum mass identified by the decomposition algorithm is set by the brightness temperature threshold, the spectral resolution, the beam size, and the distance to the cloud. Using the same constants introduced in § 4 and accounting for the clump selection criterion, the minimum clump mass is given by $M_{\rm min} = 1\ M_\odot\ (D/{\rm kpc})^2$.

The cutoff criterion (rejecting clumps smaller than 130% of the spatial or spectral resolution) causes some low-mass

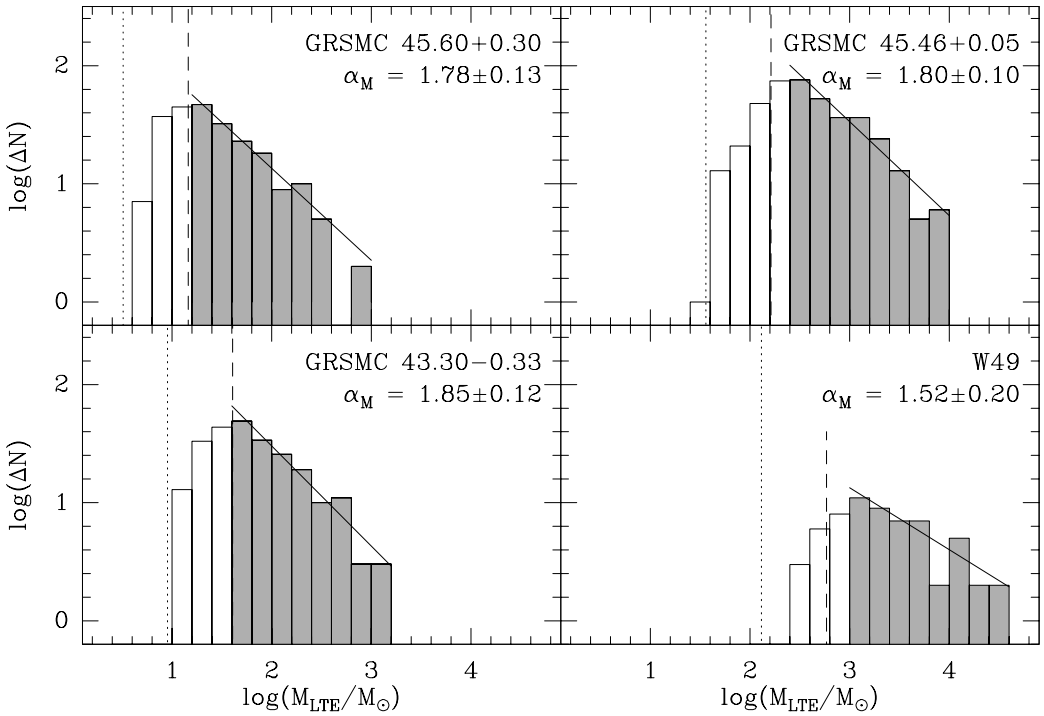

FIG. 4.—Clump mass spectra of the four GRS clouds. Only those masses above the completeness limit occupying the filled histogram columns were used in the least-squares fitting procedure to derive the power-law index α_M. The dashed line marks the value of the completeness limit. A dotted vertical line is drawn at the value of the minimum clump mass for each cloud.

clumps to be missed. Moreover, at low signal levels, noise introduces a bias to the derived clump masses. Therefore, the mass completeness limit of the decomposition is higher than the minimum detectable mass, and fits to the clump mass spectra are only reliable above the completeness limit. At the 5 σ confidence level, the completeness limit is $M_{\rm compl} = M_{\rm min} + 5\sigma_M$. The contribution to the mass due to noise, σ_M, was calculated from the mean rms brightness temperature of the data, the spectral and spatial resolution, and the distance to the cloud. Adopting the constants given in § 4, it is $\sigma_M = 0.7\ M_\odot\ (D/\mathrm{kpc})^2$. We include both the mass limit for *GAUSSCLUMPS* and the completeness limit in the panels showing the clump mass spectra (Fig. 4) as dotted and dashed lines, respectively.

Least-squares fits to $dN/dM \propto M^{-\alpha_M}$, weighted with $\Delta N^{1/2}$ for the individual mass bins, were applied to the clump mass spectra above the turnover associated with the completeness limits $M_{\rm compl}$. Mass bins used in the fitting procedure are indicated by filled histogram columns in Figure 4. The fits give values for α_M around 1.8 with high correlation coefficients (greater than 0.86; see Table 3 for a summary) and small scatter. W49 shows the largest dispersion. Within the 2 σ uncertainties, we find the same power-law relation $dN/dM \propto M^{-1.8}$ for the clump masses in each of the four clouds, independent of distance and star formation activity.

5.3. *Relations of Clump Size with Density, Line Width, and Mass*

Figures 5–8 display the relations between density, line width, and mass as a function of size for all clumps in the GRS clouds above the minimum mass discussed in the previous section. We define the clump radius as the geometric mean of the major and minor half-axes determined from *GAUSSCLUMPS*. The clump density in the top panel is determined from the LTE mass of the clump and this size.

TABLE 3

SUMMARY OF FITTED POWER-LAW RELATIONS

	Clump Radius versus Clump							
Cloud	Density α_n	Correlation Coefficients	Line Width $\alpha_{\rm lw}$	Correlation Coefficients	Mass α_m	Correlation Coefficients	Mass Spectrum α_M	Correlation Coefficients
GRSMC 45.60+0.30...	0.88(0.06)	0.71	0.15(0.06)	0.15	2.12(0.06)	0.92	1.78(0.13)	0.98
GRSMC 43.30−0.33...	0.73(0.07)	0.57	0.29(0.06)	0.26	2.27(0.07)	0.91	1.85(0.12)	0.96
GRSMC 45.46+0.05...	0.78(0.09)	0.39	0.23(0.06)	0.18	2.22(0.09)	0.77	1.80(0.10)	0.94
W49.....	0.85(0.35)	0.24	0.15(0.22)	0.07	2.15(0.35)	0.53	1.56(0.20)	0.86
Weighted mean	0.81(0.06)	...	0.22(0.07)	...	2.19(0.07)	...	1.79(0.10)	...
Virial equilibrium	1.0	...	0.5	...	2.0	...	...	...

NOTE.—Power-law slopes deduced from linear least-squares fits are followed by standard deviations in parentheses and linear correlation coefficients in the adjacent column.

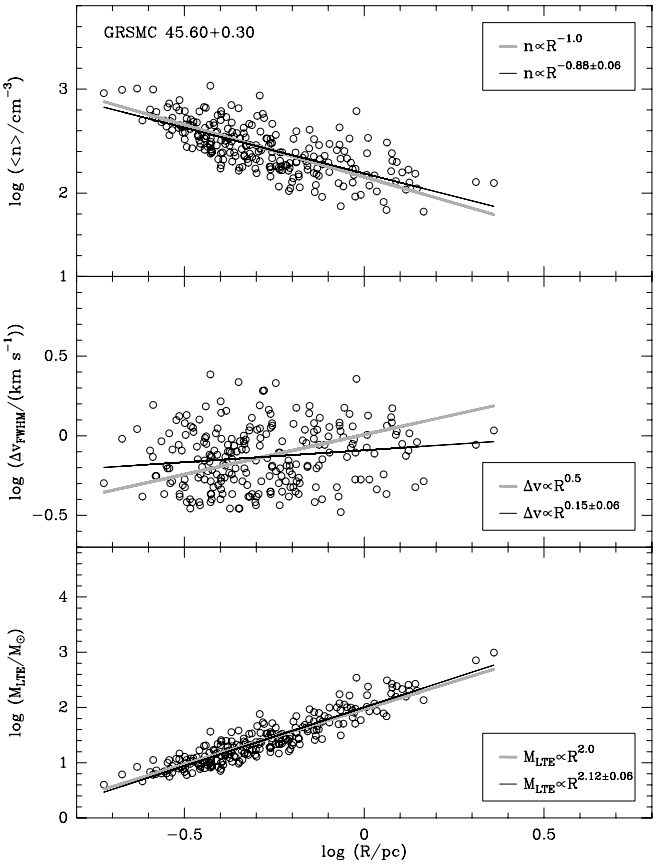

FIG. 5.—Size-density (*top panel*), size–line width (*middle panel*), and size-mass (*bottom panel*) relations for the identified clumps (*open circles*) in GRSMC 45.60+0.30. Least-squares fits to $\Delta v \propto R^{\alpha_{\rm lw}}$, $n \propto R^{-\alpha_n}$, and $M_{\rm LTE} \propto R^{\alpha_m}$ are indicated by the solid black lines. The grey lines show fits with fixed power-law indices of $\alpha_{\rm lw} = 0.5$, $\alpha_n = 1$, and $\alpha_m = 2$ corresponding to the conventional Larson relations.

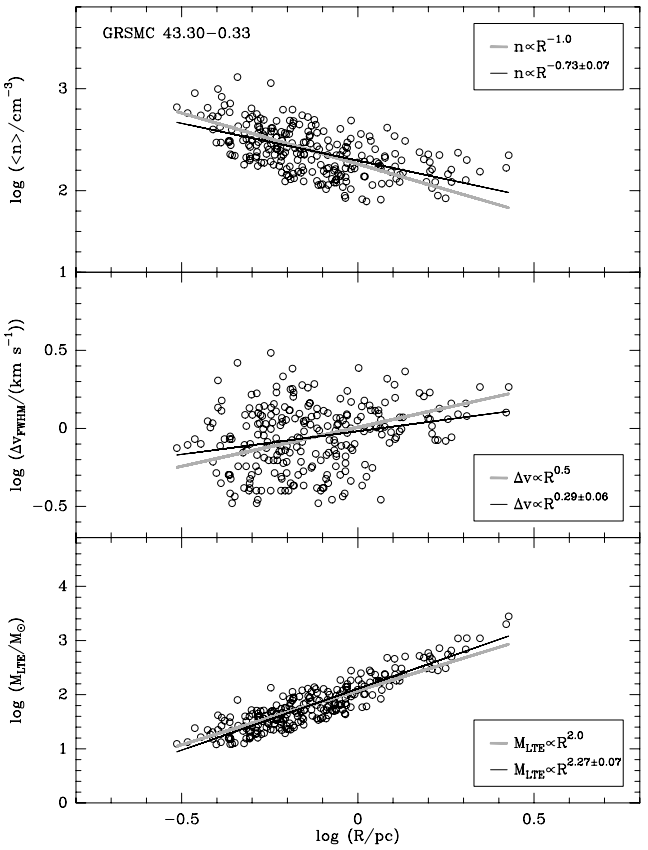

FIG. 6.—Same as Fig. 5, but for GRSMC 43.30−0.33

The contribution from the thermal line width to the observed line width may be considerable and could flatten the slope of a size–line width relation (Myers & Goodman 1988). For ^{13}CO, the thermal line width $\Delta v_{\rm th}$ in km s^{-1} can be written as $\Delta v_{\rm th} = 0.13(T/10)^{1/2}$, where T is the kinetic temperature in K. Because of the spectral smoothing and the selection criterion applied to the clumps before deconvolution (§ 4), thermal broadening for clumps with kinetic temperatures of a few times 10 K is unresolved. For a kinetic temperature of 10 K, every clump that we identify has highly supersonic line widths.

We deduced power-law indices for density, line width, and mass as a function of clump size by applying least-squares fits. In addition to the fitted relations, we include lines representing the Larson relations for virial equilibrium in the plots (see § 6.2). The fit results are summarized in Table 3, including the power-law indices for the clump mass spectra from the previous section, linear correlation coefficients, and weighted means determined from the fit results for the four clouds.

5.4. *Equilibrium State of the Clumps*

The equilibrium state of a cloud or clump can be characterized by the virial parameter $\alpha_G = M_{\rm vir}/M_{\rm LTE}$ (Bertoldi & McKee 1992), which is a measure of the ratio of kinetic to gravitational energy density. In the case of optically thin emission, clumps with Gaussian intensity distributions, as

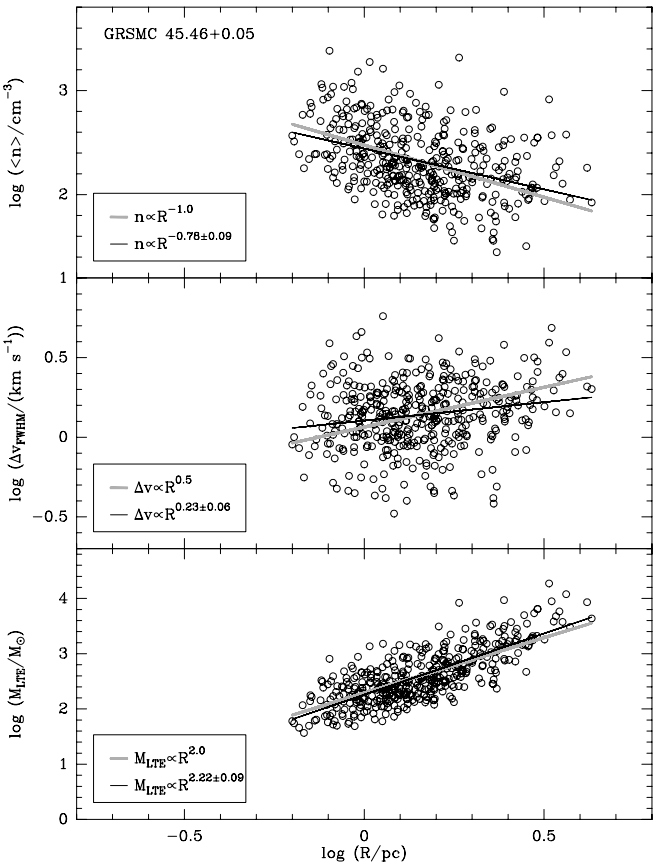

FIG. 7.—Same as Fig. 5, but for GRSMC 45.46+0.05

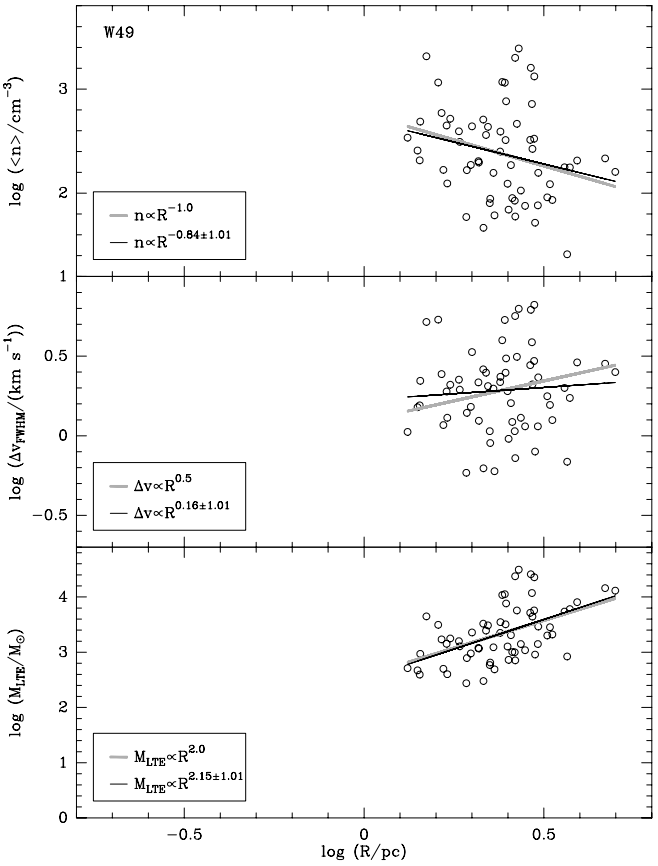

FIG. 8.—Same as Fig. 5, but for W49

fitted to the observed data cubes by *GAUSSCLUMPS*, also have Gaussian density profiles (Stutzki & Güsten 1990; Stutzki et al. 1998). We therefore use the analytical expression for a Gaussian density distribution in the virial theorem to calculate virial masses of the decomposed clumps. In the absence of external pressure and magnetic fields, the virial theorem $2T_{\rm kin} + W = 0$ for a Gaussian clump with a radial density distribution takes the form (Stutzki & Güsten 1990)

$$3M\sigma^2 - \sqrt{\frac{\ln 2}{2\pi}}\,\frac{GM^2}{R} = 0\,, \tag{5}$$

where $G = 1/232$ is the gravitational constant in units of km s^{-1}, pc, and $M_\odot$; σ denotes the velocity dispersion of the clump in km s^{-1}; and R is the radius of the clump in pc. From this, the virial mass of a clump with Gaussian density distribution can be written as

$$\frac{M_{\rm vir}}{M_\odot} = 378 R \Delta v^2\,, \tag{6}$$

with the FWHM line width $\Delta v = \sigma(8\ln 2)^{1/2}$.

Figure 9 shows the ratio of virial to LTE clump mass as a function of LTE clump mass for the ensembles of clumps in the four different clouds. As for the clump mass spectra, the distribution of LTE clump masses for each cloud reflects the distance to the complex. In all four clouds, the majority of clumps are found well above $M_{\rm vir}/M_{\rm LTE} = 1$ (Fig. 9, *dotted lines*). The dashed lines denote the mass completeness limits introduced in § 5.2 and included in Figure 4. The solid lines model the upper envelope to the data and will be discussed

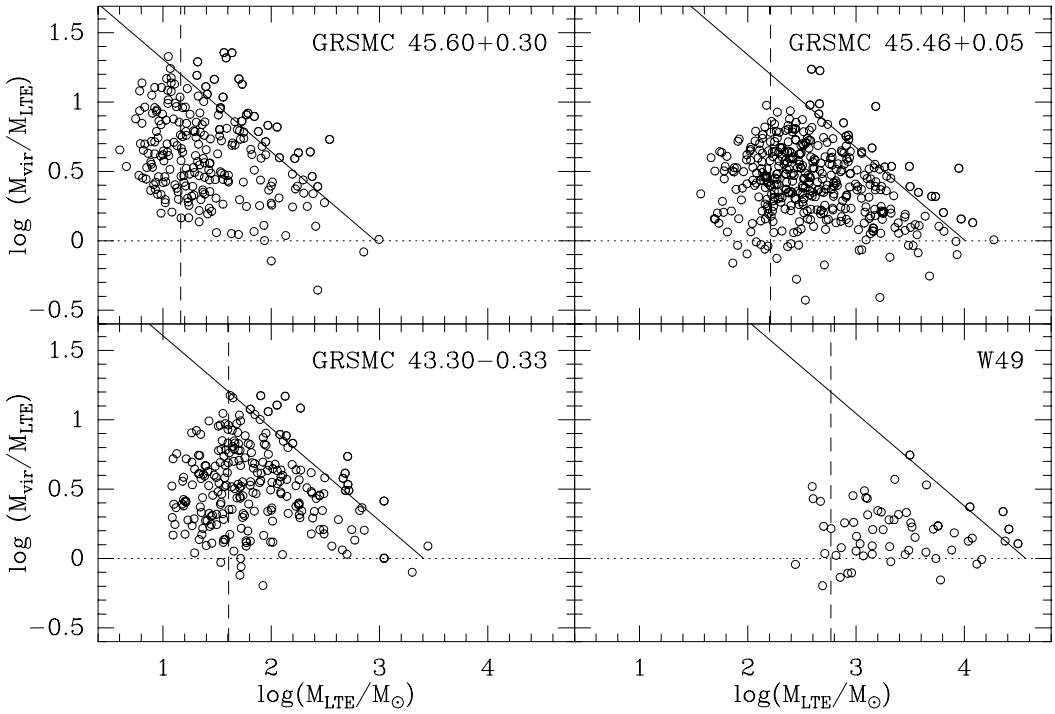

FIG. 9.—Ratio of virial to LTE mass as a function of LTE mass for the identified clumps (*open circles*) in the four GRS clouds. Dotted lines correspond to $M_{\rm vir} = M_{\rm LTE}$. Dashed lines delineate the completeness limit for $M_{\rm LTE}$ (see Fig. 4). The solid lines show the qualitative behavior of clumps with high virial parameters (see text for details) and have a slope fixed to $-\frac{2}{3}$.

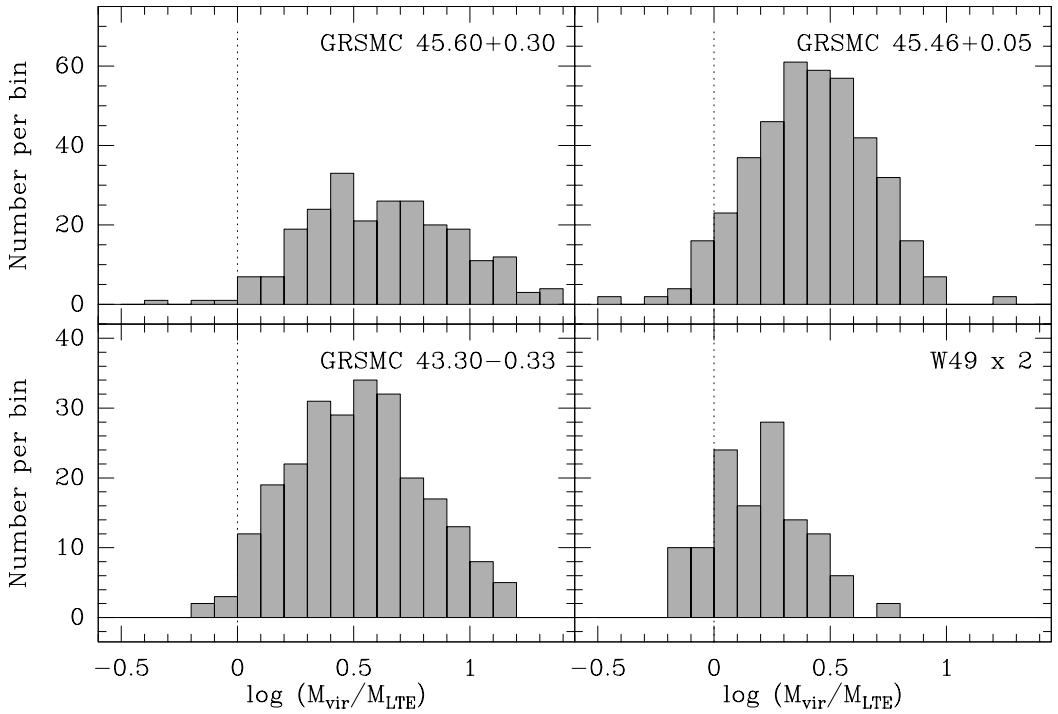

FIG. 10.—Histograms of the ratio of virial to LTE mass for the identified clumps in the four GRS clouds. As in Fig. 9, the dotted line corresponds to $M_{\rm vir} = M_{\rm LTE}$. The y-axis for W49 has been scaled down by a factor of 2.

in detail in the next sections. In order to evaluate the fraction of clumps with a certain value of the virial to LTE mass ratio, we calculated histograms of the gravitational parameter α_G for each cloud (Fig. 10).

If clumps with $M_{\rm vir}/M_{\rm LTE} > 1$ are externally bound, the pressures needed to bind the clumps can be evaluated by adding the surface term $4\pi R^3 P_{\rm ext}$ to the equation of virial equilibrium. The binding pressure of a clump in units of K cm^{-3} is then given by

$$\frac{P_{\rm ext}}{k} = 0.56\,\frac{M}{R^2}\left(378\,\frac{\Delta v^2}{R} - \frac{M}{R^2}\right), \tag{7}$$

which can be rewritten as

$$\frac{\sigma^2}{R} \propto \frac{P_{\rm ext}}{k}\,\frac{1}{N({\rm H_2})} + N({\rm H_2})\,, \tag{8}$$

where k is the Boltzmann constant. This equation describes the balance between the external pressure and the turbulent gas pressure $\rho\sigma^2$, where $\sigma = \Delta v/(8\ln 2)^{1/2}$ is the velocity dispersion of the clump in km s^{-1}, reduced by the gravitational energy density ($GM\rho/R$). It is possible to infer the magnitude of the binding pressure from a plot of σ^2/R as a function of clump column density. The corresponding plots for the GRS clouds are shown in Figure 11. External pressures are unimportant in confining high-mass clumps in gravitational virial equilibrium ($\alpha_G \sim 1$). There σ^2/R is proportional to the surface density $\Sigma = M/\pi R^2$ and hence the column density $N({\rm H_2})$. For small clump masses, where external pressures dominate and the virial parameter α_G is large, σ^2/R depends on the column density as $N({\rm H_2})^{-1}$ (Keto & Myers 1986). Figure 11 demonstrates this behavior for different values of the binding pressure.

Clumps with $P_{\rm ext}/k \simeq 0$ K cm^{-3} are gravitationally bound. Since the clumps in W49 are much closer to a ratio

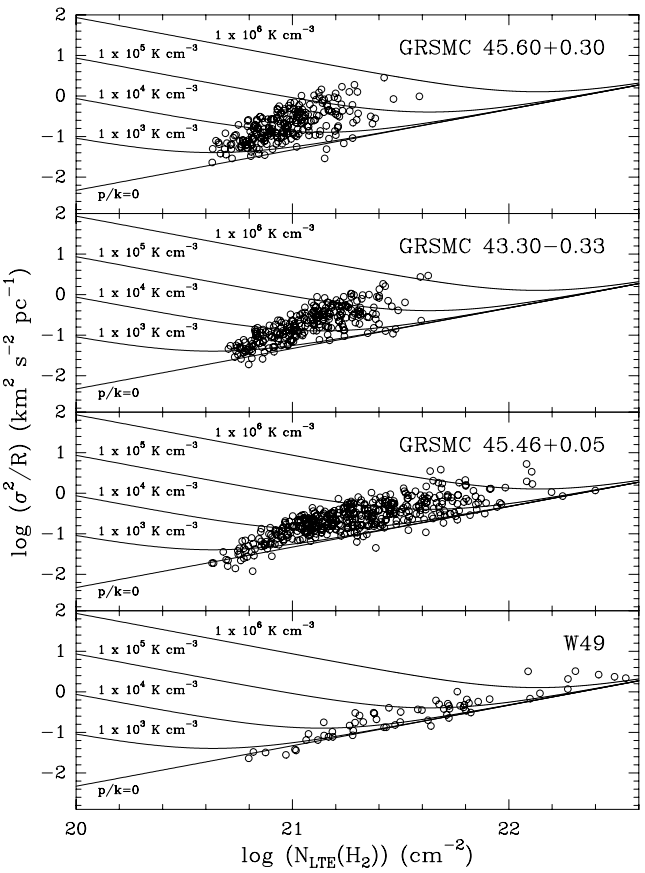

FIG. 11.—Ratio of σ^2/R as a function of clump column density $N({\rm H_2})$ for the GRS clouds. Lines of constant external binding pressure from $P/k = 0$ to 10^6 K cm^{-3} are included.

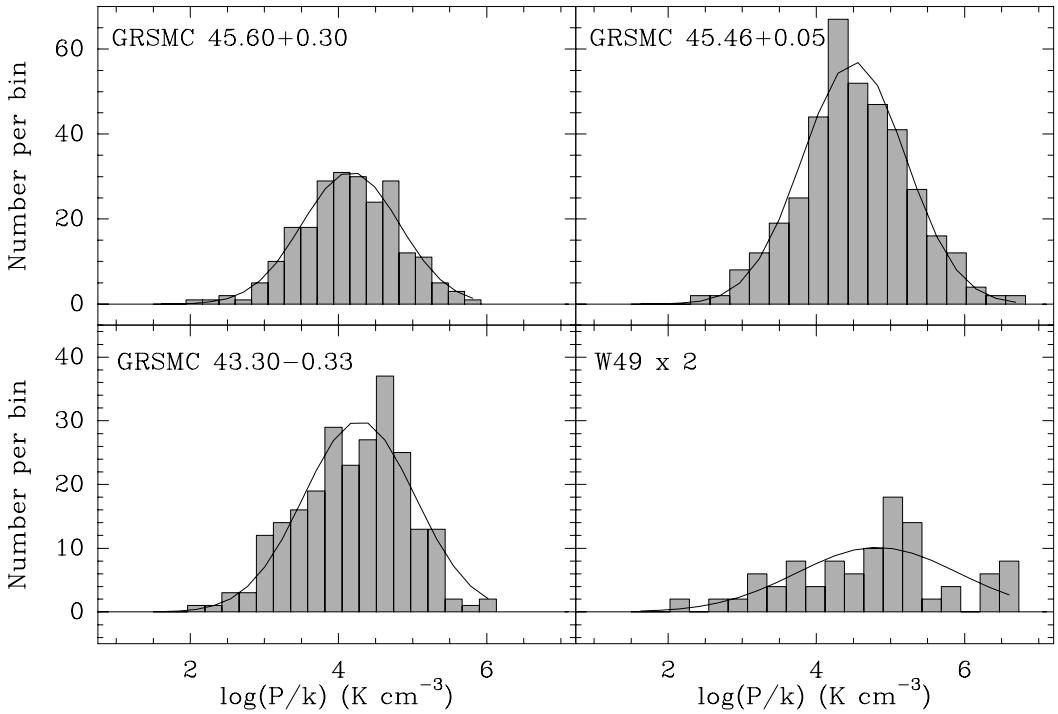

FIG. 12.—Histograms of the external pressures needed to bind the clumps in the GRS clouds. Median binding pressures given in Table 4 are deduced from the Gaussian fits to the histograms. The fits are plotted as a solid line in each panel.

$M_{\rm vir}/M_{\rm LTE}$ of unity than the majority of clumps in the other sources, a higher percentage of clumps in W49 require no or only small external pressures to be bound. Most of the clumps for the other clouds are found well above the $P_{\rm ext}/k = 0$ K cm^{-3} line, and these clumps would require larger external pressures to be bound. Alternatively, they could be unbound, transient objects. The external pressures needed to bind these internally overpressured clumps in the four GRS clouds range from 10^3 to 10^6 K cm^{-3}. Histograms of required external pressure were developed from the data in Figure 11 and are shown as Figure 12. Since gravitationally bound clumps formally have negative binding pressures, only clumps with $\alpha_G > 1$ are considered in the histograms. Median pressures deduced from the histograms are listed in Table 4. The median binding pressures are typically a few times 10^4 K cm^{-3}.

6. DISCUSSION

6.1. *Clump Mass Spectra*

We find power-law clump mass spectra of the GRS clouds that are independent of scale and star formation activity. Results for a variety of concepts to identify substructures applied to many different clouds and over at least 5 orders of magnitude in mass (e.g., Elmegreen & Falgarone 1996; Heithausen et al. 1998; Kramer et al. 1998) consistently yield clump mass spectra with power-law indices α_M between 1.5 and 1.9, also independent of star formation activity. Recent systematic studies of larger fields find higher values of α_M between 1.7 and 1.9 (Heyer & Terebey 1998; Nagahama et al. 1998), in excellent agreement with the GRS power-law index of 1.8. The turnover of all clump mass spectra at roughly 5 times the minimum mass identified by the decomposition is due to the clump selection criteria and reflects the completeness limit of the survey.

TABLE 4

PRESSURES AND CRITICAL CLUMP MASSES

Cloud	$P_{\rm clump}/k$ (K cm^{-3})	P_G/k (K cm^{-3})	$M_{\rm BE}$ ($M_\odot$)
GRSMC 45.60+0.30.....	1.5×10^4	1.2×10^4	180
GRSMC 43.30−0.33.....	2.0×10^4	1.5×10^5	500
GRSMC 45.46+0.05.....	3.2×10^4	3.9×10^5	2000
W49.....	6.7×10^4	1.0×10^6	7000

NOTE.—$P_{\rm clump}/k$ is the median pressure required to bind the clumps, and P_G/k is the pressure due to the weight of the self-gravitating complex. The last column gives estimates of the upper limits to the Bonnor-Ebert masses as described in the text.

For W49, we observe both a shallower slope of the clump mass spectrum but also the largest dispersion, which may be due to the relatively small number of clumps detected (Williams et al. 1994). The fact that we identify fractionally more high-mass and fewer low-mass clumps could be a result of the large distance, but we cannot rule out that it is an intrinsic property of this cloud. Moreover, given the wide range in velocity covered by emission, it is also possible that there is still some contribution from nearby clouds along the line of sight. H I spectra toward the W49 cloud sometimes show weak self-absorption features at velocities different from 16 km s^{-1}, but because the corresponding ^{13}CO features are faint, they probably do not significantly affect our results.

Although it is well established that stars form from molecular cloud cores, the link between the mass spectrum of clumps and the stellar initial mass function (IMF) is unclear. The power-law indices of clump mass spectra from molecular line data ($\alpha_M = 1.7$–1.9) are usually significantly smaller than that of the IMF, $\alpha_{\rm IMF} = 2.1$–2.5 (Salpeter 1955; Miller & Scalo 1979) for stellar masses between 1 and 10 $M_\odot$. The GRS results presented here confirm this finding

for clump masses down to $\sim 10\ M_\odot$ and linear scales as small as 0.3 pc in the case of GRSMC 45.60+0.30. It is not clear whether the slope of the clump mass spectra of the GRS clouds continues to the lower masses and smaller size scales involved in star formation. Kramer et al. (1998) find slopes of CO clump mass spectra similar to those found in the GRS clouds for masses down to Jupiter masses in a nearby, quiescent cloud and $\sim 1\ M_\odot$ in active star-forming regions.

In contrast, recent high spatial resolution observations of nearby clouds suggest a steeper mass spectrum for cores identified in the millimeter continuum, $\alpha_M > 2$ (Motte, André, & Neri 1999; Testi & Sargent 1998) for masses around $1\ M_\odot$ and on size scales of 0.01–0.1 pc. This slope is similar to that of the IMF in the same mass range. These results may signify a transition between large-scale cloud fragmentation and further fragmentation to cloud cores on scales relevant for star formation. Discrepancies between the clump mass spectra from dust continuum and molecular line observations, however, may also arise if inappropriate physical parameters in calculating the masses are adopted or if the material traced by dust and molecular line emission is not well coupled. Dust continuum observations usually only trace a small fraction of the total mass at considerably higher density compared to molecular line observations in a cloud, and estimates of the clump masses from the millimeter continuum strongly depend on the assumed dust temperature and emissivity law. Molecular line data, on the other hand, may suffer from depletion due to molecules freezing out onto dust grains at low temperatures. At distances of 2–10 kpc, typical length scales for star formation in the GRS clouds are only accessible with future interferometric observations. Such observations would also allow simultaneous investigations of the correlation of molecular line and continuum emission.

6.2. *Scaling Relations*

A number of different studies (e.g., Larson 1981; Myers 1983; Dame et al. 1986; Solomon et al. 1987) have found power-law relations between the size of a cloud and its velocity dispersion, density, and mass of the form $\Delta v \propto R^{\alpha_{\rm lw}}$, $n \propto R^{-\alpha_n}$, and $M \propto R^{\alpha_m}$. Values of the different power-law indices were empirically determined from GMC complexes and high-density clumps to be $\alpha_{\rm lw} = 0.5$, $\alpha_n = 1.0$, and $\alpha_m = 2.0$ extending over several orders of magnitude in scale and with a small scatter (see the reviews by Myers 1987 and Scalo 1987). The assumption of gravitational virial equilibrium $GM/R \propto \Delta v^2$ implies scaling relations of the form $\alpha_{\rm lw} = (\alpha_m - 1)/2$ and $\alpha_m = 3 - \alpha_n$, which are in agreement with the empirical values.

Previous studies resolving molecular clouds into clumps (e.g., Leung et al. 1983; Sanders et al. 1985; Dame et al. 1986; Kramer et al. 1996; Heithausen 1996; Heyer & Schloerb 1997; Williams et al. 2000) find power-law indices for clump ensembles that cover wide ranges around the slopes of the conventional scaling relations: α_n between 0.7 and 1.6, $\alpha_{\rm lw}$ between 0.2 and 0.7, and α_m between 1.7 and 2.5. Part of the large scatter is due to the limited dynamic range in clump size accessible in an individual cloud.

Similarly, the distributions of density, line width, and mass with clump size for the GRS data displayed in Figures 5–8 show considerable scatter, in particular for the size-density and size–line width relations. Accordingly, none of these slopes are well constrained.

Following the recommendations given by Isobe et al. (1990) and using their public domain computer code *SLOPES*, we applied two different least-squares regression methods to determine power-law indices and the corresponding uncertainties for the scaling relations: ordinary least-squares (OLS) regression of Y against the clump radius R and OLS bisector. Generally, the OLS method yields flatter slopes than the OLS bisector, and both fitted slopes bracket the values of the conventional scaling laws for the size-density and size–line width relations. The fitted slopes for these two relations do not agree within their $3\ \sigma$ uncertainty margins, and linear correlation coefficients are small. For the size-mass relation, the fitted slopes from both methods are steeper than the power-law index of the Larson relation for gravitational virial equilibrium. The slopes agree within their $3\ \sigma$ uncertainty margins, and linear correlation coefficients are high. In order to be consistent with previous determinations in the literature, we only report power-law slopes and standard deviations from the OLS regressions in Table 3. The table also contains the linear correlation coefficients.

The fitted power-law slopes for the size-density (α_n from 0.75 to 0.85) and size–line width ($\alpha_{\rm lw}$ from 0.15 to 0.30) relations in the GRS clouds are close to the lower limit of values reported in the literature, while the values for the size-mass relation (α_m from 2.1 to 2.3) are close to the literature upper limits. The combined size-mass and size-density relations are in agreement with $\alpha_m = 3 - \alpha_n$, which reflects the fact that the density is calculated from the mass and the effective radius according to $n \propto M/R^3$.

The correlation between size and density and between size and line width is poor. Therefore, we cannot recover reliable numbers for the corresponding power-law indices and consequently cannot judge whether the properties of the identified clumps strictly conform to the standard Larson relations. There is, however, a systematic trend to shallower size-density and size–line width relations and steeper size-mass relations compared to the conventional relations in all four GRS clouds. Moreover, while the clumps identified in the GRS data support power-law distributions of clump density and mass as a function of clump size, we do not find a significant clump size–line width relation in any of the GRS clouds. In particular, the clump line widths for the most quiescent cloud GRSMC 45.60+0.30 are independent of clump size. The clumps in W49, the most active star-forming region in our study, also show no significant size–line width relation, but the results for this cloud suffer from the low number of clumps detected.

The surface densities $\Sigma = M_{\rm LTE}/\pi R^2$ for the clumps in the GRS clouds show a weak dependence on clump size $\Sigma \propto R^{0.1-0.3}$, in contrast to the conventional Larson law for gravitational virial equilibrium ($\alpha_m = 2.0$), which implies a constant surface density for all clump sizes. Since the clump masses are calculated from the column densities times R^2, a Larson-like size-mass correlation could reflect that observations of a single molecular line select a limited column density range. Although it is only a $2\ \sigma$ effect, the deviations of our data from this Larson law, however, may be real since our clump column densities span an order of magnitude (Fig. 11) and the scatter in the size-mass relation is small. This conclusion does not depend on the method of fitting. Both linear least-squares regressions we applied yield slopes steeper than the conventional Larson relation of size and mass. Since the clump masses have been calcu-

lated using constant excitation, optical depth, and abundance, we caution that variations of these conditions within the cloud and among the clumps could account for the observed effect.

The observed line widths being independent of clump size in GRSMC 45.60+0.30 may point toward the presence of magnetic effects. If the line widths are larger than thermal and the nonthermal, turbulent part of the velocity dispersion is due to Alfvén waves, we can estimate a magnetic field strength from the observed line width. For a mean observed line width of $\Delta v = 0.63$ km s^{-1} and a thermal line width of 0.13 km s^{-1}, the observed nonthermal velocity dispersion $\sigma_{\rm NT}$ is 0.27 km s^{-1}, corresponding to an Alfvén speed $v_{\rm A} = \sigma_{\rm NT} 3^{1/2}$ of 0.47 km s^{-1}. Assuming

$$\sigma_{\rm NT}^2 = \frac{2}{3}\frac{B^2}{8\pi mn} \tag{9}$$

(Myers & Goodman 1988) and using a mean density calculated from the mass and radius of the cloud given in Table 2, the resulting magnetic field strength is 15 μG. This number is at the low end of estimates for the magnetic field strength in a variety of molecular clouds (Myers & Goodman 1988).

6.3. *Cloud and Clump Equilibrium*

Molecular clouds as a whole (Dame et al. 1986; Solomon et al. 1987) and embedded cores observed in high-density tracers (Myers 1983) are usually found to be in gravitational virial equilibrium. Power-law indices for the conventional scaling relations discussed in the previous section were initially derived from these classes of objects and reflect the relations expected for gravitational virial equilibrium.

The ratios of the virial to LTE mass for the four GRS clouds listed in Table 2 ($M_{\rm vir}^{\rm cloud}/M_{\rm int}^{\rm cloud} = 1.2$–$2.6$) support the results from other studies that molecular clouds are in or near gravitational virial equilibrium. Because virial cloud masses are upper limits (as a result of possible line broadening in an optically thick line), while the LTE cloud masses are lower limits, the virial parameters for the GRS clouds are upper limits. We therefore conclude that all four GRS clouds are gravitationally bound. This confirms the results for GRSMC 45.60+0.30, GRSMC 45.46+0.05, and W49 from earlier ^{12}CO observations (Dame et al. 1986; Solomon et al. 1987).

The equilibrium state of the clumps within clouds, observed in CO isotopomers and with high angular resolution, is found to be much more diverse. Clumps typically have ratios of virial to LTE mass well above the limit of virialization, $M_{\rm vir}/M_{\rm LTE} \simeq 1$ (e.g., Bertoldi & McKee 1992; Williams, Blitz, & Stark 1995; Heyer et al. 2001). Only a small number of high-mass clumps are strongly self-gravitating, and only a small subset of these are forming stars or have infrared point-source counterparts. Figure 9 reveals that most of the clumps in the GRS clouds GRSMC 45.60+0.30, GRSMC 45.46+0.05, and GRSMC 43.30−0.33 show the same trend and are not gravitationally bound.

Although low-mass clumps identified from observations of high-density tracers in molecular clouds are often found to be gravitationally bound, this is not in conflict with most of the low-mass CO clumps being gravitationally unbound, since observations of high-density tracers are biased toward compact and self-gravitating cores. The total mass of a clump core seen at the high densities ($n \sim 10^6$ cm^{-3}) is only a small fraction of the total mass of the same clump as seen in ^{13}CO. The corresponding ^{13}CO clump could be gravitationally bound as well, since it has a central mass condensation, but would be larger and more massive.

We suggest that the deviations of the scaling relations for the clumps in the GRS clouds from the Larson relations for gravitational virial equilibrium reflect that most of the clumps are simply not gravitationally bound. It is interesting that the clumps identified from the outer Galaxy Survey (Heyer et al. 2001) show a flat size–line width relation ($\alpha_{\rm lw} = 0.13$) for small objects with sizes between 0.7 and 7 pc that is similar to the relations found for the GRS clouds. The size–line width relation for the outer Galaxy clumps gradually steepens to $\alpha_{\rm lw} = 0.6$ for clump sizes approaching typical GMC radii (7–13 pc). Since Heyer et al. (2001) do not distinguish clumps in different cloud complexes, we suggest that the small-size clumps belong to nearby clouds that are resolved into substructures (comparable to the clumps identified in GRSMC 45.60+0.30, not in gravitational virial equilibrium, flat size–line width relation), whereas the large-size clumps belong to, or are, more distant clouds (in gravitational virial equilibrium as a whole, steeper size–line width relation).

The distributions of the virial parameter with clump mass for the clumps identified in the GRS clouds show some details that are worth noting. Bertoldi & McKee (1992), Williams et al. (1995), and Heyer et al. (2001) find a tight correlation of the virial parameter with clump mass according to $\alpha_G = (M_0/M_{\rm LTE})^{2/3}$, which is theoretically expected for gravitationally unbound, pressure-confined clumps (Bertoldi & McKee 1992). For large values of α_G and masses above the completeness limit, the virial parameters for the clumps in the GRS clouds appear to follow this relation. Since the overall distribution of the virial parameter for the clumps in the GRS clouds makes it difficult to obtain a reasonable fit to $\alpha_G = (M_0/M_{\rm LTE})^{2/3}$, we modeled this upper envelope by using a slope fixed to $-\frac{2}{3}$ and an anchor point given by the completeness limit and a high virial parameter ($\alpha_G = 16$) for each of the four clouds. The resulting solid lines included in Figure 9 are not fits to the data points but are intended to show the qualitative behavior of clumps with high virial parameters.

Although some of the clumps in the GRS clouds follow the trend of $(M_{\rm LTE})^{-2/3}$, the distributions of clumps with low masses and small virial parameter in Figure 9 are different from those in some of the previous clump decomposition studies. The clumps in the GRS clouds more regularly fill the $M_{\rm LTE}$-α_G plane, in particular for smaller masses and smaller values of the virial parameter. We attribute the finding of additional low-mass clumps with small values of the virial parameter to the higher affinity of *GAUSSCLUMPS* to smaller clumps and line widths. Since *GAUSSCLUMPS* assumes an a priori shape of the clumps, it is in principle able to disentangle even small clumps overlapping along the line of sight in space and velocity. It also has, however, the tendency to add small artificial clumps to the residuals of large, non-Gaussian features.

A distribution of virial parameters similar to those for the GRS clouds is found by Kramer et al. (1996), who also used *GAUSSCLUMPS* to decompose emission from their Orion B data set. Other decomposition algorithms assign lower level emission to larger, more massive clumps, resulting in a lack of low-mass clumps. Below the completeness limit, values for the virial parameter in the GRS clouds tend to be lower because of clump selection and sensitivity effects,

which result in a lack of low-mass clumps with high virial masses.

The ratio $M_{\rm vir}/M_{\rm LTE}$ for W49 is independent of clump mass, and all, even the smaller, identified clumps appear to be self-gravitating. As a result of the large distance to W49, a number of unresolved clumps may be blended together to be confused with a single high-mass clump. The virial parameter of such a clump will be dominated by the most massive subclumps, which, in light of the high star formation activity in W49, are likely to be self-gravitating and hence have virial parameters around unity.

In order to examine the effects of distance on the equilibrium state of clumps identified by the decomposition, we smoothed our data for the most quiescent cloud GRSMC 45.60+0.30 to represent a 5 times larger distance (9 kpc). The clumps found in these low angular resolution data are plotted as filled triangles in Figure 13 together with the high angular resolution clumps (*open circles*) and the clumps in W49 (*crosses*) from Figure 9. The qualitative behavior of the low-resolution clumps in GRSMC 45.60+0.30 is preserved from the high-resolution data. Even at the 5 times poorer angular resolution, most of the newly identified clumps remain gravitationally unbound. Clearly, the equilibrium properties of the clumps in W49 are fundamentally different from those of the clumps in GRSMC 45.60+0.30. We attribute these different clump properties to the differences in star formation activity between the two clouds.

According to the standard scaling relations for objects in gravitational virial equilibrium, the clumps in W49 should show a well-defined size–line width relation, which is not observed. The observed flat size–line width relation may arise if initially virialized clumps undergo contraction. In this case, the sizes of the clumps will be reduced and the line widths increased, resulting in a flattening of the size–line width relation. The presence of a flat size–line width relation among some very active star-forming molecular clouds was first noticed and interpreted in the above sense by Larson (1981).

6.4. *The Role of External Pressure*

Star formation should occur in clouds whose clumps have dynamical timescales much smaller than that of the cloud itself and if the binding energies, resulting from gravity and external pressure, dominate the internal energies of thermal and nonthermal motions. A typical dynamical timescale for the cloud as a whole is the crossing time $t_{\rm cross} = R/\sigma_v = 2.35\langle R\rangle/\Delta v$ Myr. Using the cloud radii and global line widths listed in Table 2, $t_{\rm cross}$ is 5–10 $\times$ 10^6 yr. Dynamical timescales for the clumps inside clouds are much smaller, typically 10^4–10^5 yr. Undriven interstellar turbulence decays quite rapidly, on timescales of the order of or shorter than the free-fall time of the system (see the results of MHD simulations by, e.g., Mac Low et al. 1998; Stone, Ostriker, & Gammie 1998; Klessen, Heitsch, & Mac Low 2000). The simulations together with the observed highly supersonic line widths suggest that if turbulence supports molecular clouds against star formation, it must be constantly driven or large molecular clouds would be transient, efficiently star-forming objects. Clumps that are not self-gravitating will be rapidly dispersed unless confined by external pressure since their dynamical timescale is much smaller than that of the cloud and the random, turbulent flow that creates local density enhancements can also disperse them.

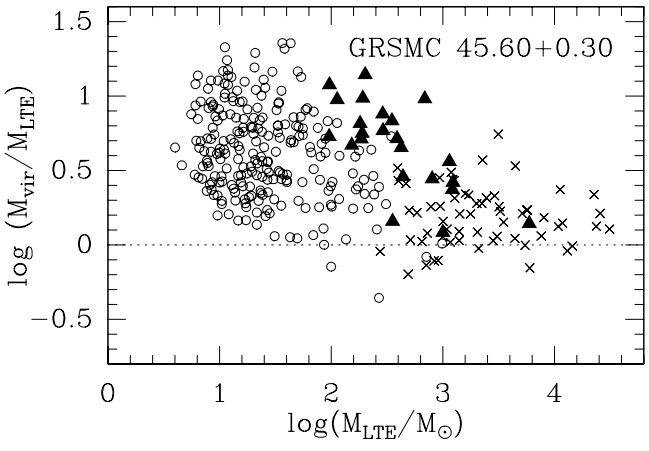

FIG. 13.—Ratio of virial to LTE mass as a function of LTE mass for the clumps in GRSMC 45.60+0.30 with the original angular resolution (*open circles*) and clumps identified after smoothing to a 5 times larger beam (*filled triangles*). Crosses represent the clumps found in W49. The dashed line corresponds to $M_{\rm vir} = M_{\rm LTE}$.

The observed large number of clumps with high virial parameters implies that they are either unbound, dispersed, and reformed anew at a high rate or else bound by external pressure. Bertoldi & McKee (1992) suggest the latter to be the case since the magnitude of external pressures they estimate for the clouds in their study is similar to the required binding pressures for the clumps.

We cannot ascertain whether the gravitationally unbound clumps we find are transient or confined by external pressure. We can, however, estimate and compare the magnitudes of the possible sources of external pressure and examine their possible role in confining the clumps.

For the purpose of this discussion, we assume that molecular clouds are embedded in an ambient medium of low density (intercloud medium, predominantly atomic) and that the clouds themselves consist of a low-density interclump medium filling most of the cloud volume (probably also predominantly atomic) and containing embedded, higher density, molecular clumps. The sharp boundaries observed in molecular tracers including CO are mainly due to the limited sensitivity of the observations and a sharp phase transition from molecular to atomic gas, rather than to a sharp density gradient at the edge of the clouds.

The pervasive, ambient intercloud medium could then provide part of the pressure needed to bind the clumps. The pressure of the ambient interstellar medium (ISM) is about 3×10^4 K cm^{-3} in the solar vicinity (Boulares & Cox 1990), of which $\sim 1 \times 10^4$ K cm^{-3} is due to magnetic pressure and cosmic rays. Since most of the intercloud and interclump medium is probably atomic, Heyer et al. (2001) propose that a large fraction of the external pressure in the Galactic plane could be due to the weight of the atomic layer in the disk. They estimate a pressure due to H I of $\sim 2 \times 10^4$ K cm^{-3} for the outer Galaxy, very similar to the solar neighborhood estimates. Because of a higher mass surface density of atomic gas in the inner Galaxy, this pressure could be somewhat higher there. Confusion due to the warm H I background at all velocities in the plane of the inner Milky Way, however, makes it difficult to estimate the total H I column associated with the individual clouds in the GRS. We can only determine the H I opacity along lines of sight showing self-absorption at a cloud's LSR velocity, when cold H I is intimately associated with molecular gas. There-

fore, we cannot determine the weight of the H I associated with the intercloud or interclump media directly. In the following, we assume that the total pressure of the ambient intercloud gas for the GRS clouds does not exceed a few times 10^4 K cm^{-3}.

Since the clouds are self-gravitating, the weight of the overlying material in the cloud could provide a significant fraction of the binding pressure for the clumps (Bertoldi & McKee 1992). If we neglect magnetic fields and embedded stellar objects, which support the clouds against gravity, the pressure inside a cloud is the surface pressure of the ambient ISM plus the pressure due to the self-gravity of the cloud. Considering only gas pressure and no other forces, the virial theorem reduces to (Bertoldi & McKee 1992)

$$3P_G V = -W = \frac{3}{5} a \frac{GM^2}{R}, \tag{10}$$

where P_G is the effective mean pressure, or "gravitational pressure" (Bertoldi & McKee 1992), provided by the weight of the material in a cloud with volume V, mass M, and radius R. Since the gravitational energy W is derived from an integral over the density distribution, P_G depends on the geometry and the density profile of the cloud, which is accounted for by the numerical factor a. This factor is of order unity and has been evaluated in detail by Bertoldi & McKee (1992). For simplicity, we use the volume of a spherical cloud with radius $\langle R \rangle$ and a $1/r$ density profile for which $a = 10/9$. In this case, a is within 75% of the extreme values for the density laws given in § 5. We calculate the gravitational pressures from the surface density $\Sigma = M/\pi\langle R \rangle^2$ (using cloud masses and radii listed in Table 2):

$$P_G = \frac{1}{5} a \frac{GM^2}{V\langle R \rangle} = \frac{\pi}{6} G\Sigma^2 . \tag{11}$$

The resulting gravitational cloud pressures are compared to values of the median binding pressure of the clumps for the GRS clouds in Table 4.

The clumps in GRSMC 45.60+0.30 could be in pressure equilibrium with either the pressure of the ambient ISM or the pressure due to the weight of the cloud complex. The pressures needed to bind most of the clumps in GRSMC 43.30−0.33 and, in particular, in the more active star-forming regions GRSMC 45.46+0.05 and W49 are significantly higher than estimates for the pressure of the ambient ISM alone. Considering the uncertainties, we believe that the derived gravitational pressures for all four clouds are sufficient to bind most of the identified clumps.

If the weight of the molecular complex confines the clumps, the pressure required to bind the clumps should vary with the location of the clump within the gravitational potential. Clumps closer to the center of the cloud should feel more weight and a higher pressure. In order to test this, we computed the potential for each clump relative to the other clumps according to

$$\Phi_i = -G \sum_{j=1, i\neq j}^{N} \frac{M_j}{|r_i - r_j|} . \tag{12}$$

We do not find any correlation of Φ_i with the binding pressures in the GRS clouds. The reason for this may be that, since the distances between the clumps were calculated from the projected positions of the clumps, the uncertainties in the individual contributions to Φ_i can be quite large. A lack of correlation therefore does not rule out the pressure-confined clump scenario. More sensitive analyses are needed to test whether there are variations of the clump binding pressures within the gravitational potentials in the clouds.

Under the assumption that all clumps for which self-gravity is unimportant ($\alpha_G \gg 1$) are bound by external pressure, Bertoldi & McKee (1992) derive a relation between the virial parameter, the critical mass of a nonmagnetic isothermal clump (the Bonnor-Ebert mass $M_{\rm BE}$), and the clump mass: $\alpha_G \propto (M_{\rm BE}/M_{\rm LTE})^{2/3}$. The Bonnor-Ebert mass is given by (Spitzer 1968)

$$M_{\rm BE} = 1.18 \frac{\sigma^4}{(G^3 P_0)^{1/2}} , \tag{13}$$

where $P_0 = \rho\sigma^2$ is the turbulent clump gas pressure. Clumps whose masses exceed this critical mass are expected to be strongly self-gravitating and to have central mass condensations.

Using clump decompositions of four different ^{13}CO data sets, Bertoldi & McKee (1992) showed that the virial parameters of the clumps in the clouds follow the theoretically expected relation $\alpha_G \propto M_{\rm LTE}^{-2/3}$ and support the constancy of the critical mass for the gravitationally unbound clumps. As already discussed in the previous section, we only see this trend in an upper envelope to the clumps with high virial parameters in the GRS clouds (Fig. 9, *solid lines*). We can use the lines of constant slope that model the upper envelope to estimate upper limits to the critical mass for each cloud. Defining M_0 as the mass where $(M_0/M_{\rm LTE})^{2/3}$ intercepts $\alpha_G = 1$, the critical clump mass is given by $M_{\rm BE} = 0.20 M_0$ (Bertoldi & McKee 1992). Values of the upper limits to the critical masses for the four clouds are listed in Table 4.

A typical Bonnor-Ebert mass for gravitationally unbound clumps found in the outer Galaxy Survey is 1000–2000 $M_\odot$ (Heyer et al. 2001), which is larger than the upper limits for the quiescent GRS clouds GRSMC 45.60+0.30 and GRSMC 43.30−0.33. Since the critical mass is inversely proportional to the required binding pressures for the clumps, this could point to a higher external pressure in the inner Galaxy. Indeed, the median binding pressures derived from these two GRS clouds are higher than the median pressure required for objects from the outer Galaxy Survey (6.7×10^3 K cm^{-3}; Heyer et al. 2001). If the clumps are not transient but confined by external pressure, these confining pressures are higher in the two GRS clouds. It is, however, not clear whether the external pressure of the ambient ISM is higher in the inner Galaxy or if the clouds we selected are just more massive, resulting in higher pressures due to the overlying weight of the cloud.

Since the above analysis of the critical mass is only valid for clumps with $\alpha_G \gg 1$, the results for the active star-forming regions GRSMC 45.46+0.05 and W49 have to be treated with caution. A higher critical mass for these clouds does not correspond to a lower external binding pressure (the opposite trend is seen in the histograms in Fig. 10), but rather to a higher fraction of gravitationally bound clumps and higher clump line widths in these clouds (Figs. 5–8, *middle panels*).

7. CONCLUSIONS

Four molecular clouds contained in the ^{13}CO GRS data set were selected for a study of cloud structure. We selected

clouds spanning a range of star formation activity from the quiescent, probably non–star-forming cloud GRSMC 45.60+0.30 to W49, the most luminous star-forming region in the Galaxy. A three-dimensional Gaussian decomposition algorithm was used to identify clumps inside each cloud and to derive the clump properties as traced in ^{13}CO. To resolve the kinematic distance ambiguity and separate clouds along the same lines of sight at different or even overlapping velocities, we used results from a technique that combines self-absorption in atomic hydrogen with GRS ^{13}CO line emission (Jackson et al. 2001).

We find no differences in the shape of the clump mass spectra for the four clouds over a wide range of clump masses and star formation activity. The observed values of the clump mass power-law spectral index ($\alpha_M \sim 1.8$) show a small scatter and lie at the high end of the range spanned by other studies. This is likely to be a direct result of the high spatial dynamic range, the high sensitivity to smaller clouds, and the complete sampling of the GRS.

Similarly, we do not find significant differences among the four clouds in the slopes of the relations of density, line width, and clump mass as a function of clump size. Although the power-law indices of the size-density and size–line width relations are not well constrained, we find systematically flatter slopes compared to the conventional Larson scaling laws in all four GRS clouds. The size-mass relations are steeper than the corresponding Larson law, which may indicate a weak dependence of the clump surface density with size.

Analyses of cloud and clump equilibria show that as a whole the cloud complexes are gravitationally bound but the majorities of the clumps comprising three of the four complexes are not. This could explain the observed deviations of the scaling relations in these clouds from the standard Larson relations, which were initially established for clouds and high-density cores in gravitational virial equilibrium.

W49 is different in that the majority of the identified clumps are gravitationally bound. Considering the high star formation rate in W49, this may be an intrinsic property of the cloud and not due to its large distance. Smoothing our data for the quiescent region GRSMC 45.60+0.30 to approximately the same distance as W49 supports this conclusion since the smoothing did not change the equilibrium properties of the newly identified clumps. The high star formation rate in W49 could also account for the observed flat size–line width relation if the clumps have undergone significant contraction.

Although the mean pressure of the ISM is sufficient to bind many clumps, it is insufficient to bind the clumps with the highest values of α_G, which may be transient objects. These clumps are possibly confined by the additional external pressure provided by the weight of the gravitationally bound complexes. In all four clouds, the magnitude of the pressure due to the overlying weight of the complex is larger than estimates of the pressure of the ambient ISM alone and is sufficient to bind most of the clumps. The median binding pressures for the clumps in the GRS clouds are higher than the binding pressures required for clumps in the outer Galaxy.

There are a number of differences between the star-forming and quiescent clouds. The mean cloud densities are higher in the star-forming regions. We find a higher fraction of gravitationally bound clumps in the star-forming regions. The size–line width relation for the most quiescent cloud GRSMC 45.60+0.30 is independent of clump size. The external pressures needed to confine the gravitationally unbound clumps in the clouds are higher for the star-forming clouds, but the overlying pressure provided by the weight of the complex is also larger in a star-forming region.

The Galactic Ring Survey acknowledges support by the NSF via grant AST-9800334. The Boston University Arecibo Observatory H I Galactic Survey was supported by NSF grant AST-8511844. The Five College Radio Astronomy Observatory is supported by NSF grant AST-9725951. We thank Merissa Rudkin and Mickey Kolpak for their help with the data analysis.

REFERENCES

Adler, D. S., Lo, K. Y., Wright, M. C. H., Rydbeck, G., Plante, R. L., & Allen, R. J. 1992, ApJ, 392, 497
Allen, C. W. 1973, Astrophysical Quantities (3d ed.; London: Athlone Press)
Bertoldi, F., & McKee, C. F. 1992, ApJ, 395, 140
Blake, G. A., Sutton, E. C., Masson, C. R., & Phillips, T. G. 1987, ApJ, 315, 621
Boulares, A., & Cox, D. P. 1990, ApJ, 365, 544
Clemens, D. P. 1985, ApJ, 295, 422
Dame, T. M., Elmegreen, B. G., Cohen, R. S., & Thaddeus, P. 1986, ApJ, 305, 892
Dame, T. M., et al. 1987, ApJ, 322, 706
Elmegreen, B. G., & Falgarone, E. 1996, ApJ, 471, 816
Evans, N. J., II, Davis, J. H., Mundy, L. G., & Vanden Bout, P. 1987, ApJ, 312, 344
Falgarone, E., Phillips, T. G., & Walker, C. K. 1991, ApJ, 378, 186
Gwinn, C. R., Moran, J. M., & Reid, M. J. 1992, ApJ, 393, 149
Heithausen, A. 1996, A&A, 314, 251
Heithausen, A., Bensch, F., Stutzki, J., Falgarone, E., & Panis, J. F. 1998, A&A, 331, 65
Heyer, M. H., Carpenter, J. M., & Snell, R. L. 2001, ApJ, in press
Heyer, M. H., & Schloerb, F. P. 1997, ApJ, 475, 173
Heyer, M. H., & Terebey, S. 1998, ApJ, 502, 265
Ho, P. T. P., & Townes, C. H. 1983, ARA&A, 21, 239
Isobe, T., Feigelson, E. D., Akritas, M. G., & Babu, G. J. 1990, ApJ, 364, 104
Jackson, J. M., Bania, T. M., Simon, R., Clemens, D. P., & Heyer, M. H. 2001, ApJ, submitted
Keto, E. R., & Myers, P. C. 1986, ApJ, 304, 466
Klessen, R. S., Heitsch, F., & Mac Low, M.-M. 2000, ApJ, 535, 887
Kramer, C., Stutzki, J., Röhrig, R., & Corneliussen, U. 1998, A&A, 329, 249
Kramer, C., Stutzki, J., & Winnewisser, G. 1996, A&A, 307, 915
Langer, W. D., & Penzias, A. A. 1990, ApJ, 357, L477
Larson, R. B. 1981, MNRAS, 194, 809
Leung, C. M., Kutner, M. L., & Mead, K. N. 1983, ApJ, 262, 583
Mac Low, M.-M., Klessen, R. S., Burkert, A., & Smith, M. D. 1998, Phys. Rev. Lett., 80, 2754
Martin, H. M., Hills, R. E., & Sanders, D. B. 1984, MNRAS, 208, 35
Miesch, M. S., Scalo, J., & Bally, J. 1999, ApJ, 524, 895
Miller, G. E., & Scalo, J. M. 1979, ApJS, 41, 513
Motte, F., André, P., & Neri, R. 1999, A&A, 336, 150
Myers, P. C. 1983, ApJ, 270, 105
———. 1987, in Interstellar Processes, ed. D. J. Hollenbach & H. A. Thronson (Dordrecht: Reidel), 71
Myers, P. C., & Goodman, A. A. 1988, ApJ, 329, 392
Nagahama, T., Mizuno, A., Ogawa, H., & Fukui, Y. 1998, AJ, 116, 336
Rosolowsky, E. W., Goodman, A. A., Wilner, D. J., & Williams, J. P. 1999, ApJ, 524, 887
Salpeter, E. E. 1955, ApJ, 121, 161
Sanders, D. B., Clemens, D. P., Scoville, N. Z., & Solomon, P. M. 1986, ApJS, 60, 1
Sanders, D. B., Scoville, N. Z., & Solomon, P. M. 1985, ApJ, 289, 373
Scalo, J. M. 1987, in Interstellar Processes, ed. D. J. Hollenbach & H. A. Thronson (Dordrecht: Reidel), 349
Snell, R. L., Goldsmith, P. F., Erickson, N. R., Mundy, L. G., & Evans, N. J., II 1984, ApJ, 276, 625
Solomon, P. M., Rivolo, A. R., Barrett, J., & Yahil, A. 1987, ApJ, 319, 730
Spitzer, L. 1968, in Nebulae and Interstellar Matter, ed. B. Middlehurst & L. H. Aller (Chicago: Univ. Chicago Press), 1
Stark, A. A., Bally, J., Knapp, G. R., & Wilson, R. W. 1988, in Molecular Clouds in the Milky Way and External Galaxies, ed. R. S. Snell & J. S. Young (New York: Knudsen), 303

Stone, J. M., Ostriker, E. C., & Gammie, C. F. 1998, ApJ, 508, L99
Störzer, H., Stutzki, J., & Sternberg, A. 1996, A&A, 310, 592
Stutzki, J. 1998, in Proc. 3d Cologne-Zermatt Symp., The Physics and Chemistry of the Interstellar Medium, ed. V. Ossenkopf, J. Stutzki, & G. Winnewisser (Herdecke: GCA), 203
Stutzki, J., Bensch, F., Heithausen, A., Ossenkopf, V., & Zielinsky, M. 1998, A&A, 336, 697
Stutzki, J., & Güsten, R. 1990, ApJ, 356, 513
Tauber, J. A., Goldsmith, P. F., & Dickman, R. L. 1991, ApJ, 375, 635
Testi, L., Felli, M., & Taylor, G. B. 1999, A&AS, 138, 71
Testi, L., & Sargent, A. I. 1998, ApJ, 508, 91
Ungerechts, H., Umbanhowar, P., & Thaddeus, P. 2000, ApJ, 537, 221
Vogelaar, M. G. R., & Wakker, B. P. 1994, A&A, 291, 557
Welch, Wm. J., Dreher, J. W., Jackson, J. M., Terebey, S., & Vogel, S. N. 1987, Science, 238, 1550
Williams, J. P., Blitz, L., & McKee, C. F. 2000, in Protostars and Planets IV, ed. V. Mannings, A. P. Boss, & S. S. Russell (Tucson: Univ. Arizona Press), 97
Williams, J. P., Blitz, L., & Stark, A. A. 1995, ApJ, 451, 252
Williams, J. P., De Geus, E. J., & Blitz, L. 1994, ApJ, 428, 693
Wouterloot, J. G. A., Brand, J., Burton, W. B., & Kwee, K. K. 1990, A&A, 230, 21